Mi, J.; Nathan, Graham Jerrold.
Statistical analysis of the velocity field in a mechanical precessing jet flow, *Physics of Fluids*, 2005; 17 (1):015102-1-015102-17.

Statistical analysis of the velocity field in a mechanical precessing jet flow

J. Mi and G. J. Nathan
School of Mechanical Engineering, University of Adelaide, South Australia 5005, Australia

(Received 24 June 2004; accepted 1 October 2004; published online 1 December 2004)

An experimental investigation of a precessing jet issuing from a mechanically rotating nozzle directed at an angle of $\alpha=45°$ relative to the axis of rotation is reported. Both conventional and conditional statistics of the velocity field of the jet were measured using a combined hot-wire and cold-wire (to identify any reverse flow) probe. Three distinct values ($\approx$0.005, 0.01, and 0.02) of the precession Strouhal number St_p ($\equiv$ rotation frequency $\times$ nozzle diameter / jet exit bulk velocity) were used to assess the effect of varying St_p. The measurements reveal that the Strouhal number in general has significant influence on the entire mixing field generated by a precessing jet. The occurrence of precession at all the Strouhal numbers of investigation produces a central recirculation zone at $x \leqslant 7d$, where x is a distance measured from the rotating nozzle exit. A critical Strouhal number, i.e., $\mathrm{St}_{p,cr} \approx 0.008$ for the present case, is identified: at $\mathrm{St}_p \geqslant \mathrm{St}_{p,cr}$ the core jet converges to the axis of rotation while at $\mathrm{St}_p \geqslant \mathrm{St}_{p,cr}$ it does not. The characteristics of the turbulent flow in the near and intermediate regions are quite different and depend upon the magnitude of St_p. The near-field region, $x/d \leqslant 10-15$, is dominated by a regime of global precession of the entire jet. As a result, the large-scale entrainment of the ambient fluid is substantially enhanced while the fine-scale turbulent mixing is suppressed. Under the supercritical regime (i.e., $\mathrm{St}_p \geqslant \mathrm{St}_{p,cr}$), the jet in the far field resembles some features of the nonprecessing counterpart. Nevertheless, significant differences still retain in the statistical properties. © *2005 American Institute of Physics*.
[DOI: 10.1063/1.1824138]

I. INTRODUCTION

The statistically steady turbulent jet issuing from a round nozzle into a large stagnant or low speed coflowing surroundings has been investigated extensively by means of experiments, numerical simulations, and analysis. The turbulent mixing characteristics of this flow has been a dominant theme of such research because it is relatively simple in geometry and also a basic component in many practical systems. In the meantime, numerous investigations have also sought to substantially alter the mixing characteristics of a jet with view to benefiting performance for a range of applications. This has resulted in more complex systems which include features such as swirl (e.g., Syred and Beer,[1]), bluff body recirculation (e.g., Gutmark *et al.*[2]) and various types of "excited" jet devices (e.g., Refs. 3–6).

One method for manipulating jet mixing is by large-scale, low-frequency oscillations of the entire jet of which jet precession is one example. The term "precession" originates from planetary motions and describes the periodic motion of one axis (that of the jet) about another (here that of the nozzle). This term appears to have first been discussed with regard to jet flows by Nathan[7] although it was used earlier to describe the unsteady motion of a vortex core in swirling flows.[1] The Strouhal number of these low-frequency oscillations, $\mathrm{St}=fd/U_e$ (where f, d, and U_e denote the oscillation frequency, exit diameter, and mean velocity of the jet, respectively), is one to two orders of magnitude lower than that of the dominant frequency of the vortex formation within the shear layer of an emerging jet, $\mathrm{St} \approx 0.3-0.5$ (e.g., Refs. 8 and 9). In contrast to acoustic excitation, which seeks to excite the "preferred mode" of these dominant vortex shedding patterns, low-frequency excitation causes a large-scale oscillation of the entire jet. There is some evidence that such oscillations may be naturally present, although weak, within an unexcited jet.[10]

Precessing jet (PJ) flows can be generated through a self-exciting, fluid-mechanical (fluidic) device that has found application as an industrial burner.[11,12] In unconfined gaseous flames, it acts to increase the radiant fraction, or radiant heat transfer from a flame, so reducing the global flame temperature and thermal NO_x emissions relative to a wide range of flames produced by equivalent swirl, bluff body, and simple jet burners.[13] Pilot-scale trials[14] have demonstrated similar benefits in higher temperature environment with the air preheated to temperatures of up to 840 °C. Full-scale installations of commercial PJ burner systems in rotary kilns (15–120 MW) have consistently demonstrated that, relative to the flames from the burners they replaced, NO_x emissions are reduced by 30%–70% while the fuel saving is typically 5% (e.g., Refs. 15–18). More recently this flow has also been shown to provide benefits in applications involving pulverized solid fuels.[19–21]

While the efficacy of the PJ flow is proven in practice, it is a flow that is extraordinarily difficult to study at the fundamental level. Primarily this is due to the underlying significance of a large-scale unsteady oscillation which necessarily also results in the flow being statistically unsteady. While recent progress has been made in quantifying the phase-averaged flow within, and emerging from, the fluidic PJ nozzle,[22,23] it remains difficult to analyze. The complexity of the flow within the chamber results in an emerging jet

which is highly noncircular and oscillates with large cycle-to-cycle variations. In addition, the Strouhal number of the oscillation cannot be varied significantly without changing nozzle dimensions (e.g., chamber length[24]) and this change also alters other aspects of the flow, such as jet exit "diameter." To allow a more fundamental investigation of the effects of precession on the mixing and combustion characteristics of a well-defined jet, the Turbulence, Energy & Combustion Group of the University of Adelaide has devised a mechanically rotated PJ nozzle. Unlike the flow from the fluidic PJ nozzle, the mechanical precessing jet (MPJ) has well-defined initial conditions, each of which can be varied independently.

The MPJ has been investigated in both reacting and nonreacting conditions. Nathan *et al.*[25] investigated the effect of varying the Strouhal number of precession, $\mathrm{St}_p = f_p d / U_e$ (where f_p, d and U_e denote the precession frequency, exit diameter, and mean velocity of the jet, respectively) on the global performance of open jet flames of methane and propane. They found that, by changing St_p with all other parameters held constant it is possible to produce a wide range of different flame types from yellow to blue. They classified the short, broad, blue flames as having a "low" Strouhal number, and the longer, yellower flames as having a "high" Strouhal number. In the high St_p regime ($\mathrm{St}_p > 0.01$) the radiant fraction was increased by $\sim$15% and the NO_x emissions reduce by 25% relative to a conventional jet diffusion flame. In this regime the flame shape and global characteristics are similar to those obtained from comparable measurements with the fluidic PJ burners.[13]

Schneider[26] and Schneider *et al.*[27,28] have investigated the nonreacting velocity and pressure within the flow from a MPJ nozzle using both laser Doppler anemometry (LDA) and a miniature four-hole "Cobra" Pitot-tube probe. They employed a phase-averaging scheme, referenced to the phase of the nozzle, to identify flow patterns and structure for $\mathrm{Re}_d = 26\,600$ and $\mathrm{St}_p \approx 0.015$. They showed that the jet spirals out from the nozzle to form a helix around a recirculation flow zone. They identified large gradients in the trajectory of the emerging jet, both in the azimuthal and radial directions, associated with the presence of a low-pressure core that precesses with the jet, but with a slight phase lag. While the entire near-field flow, typically $x/d \leqslant 6$, was found to precess with the jet, no evidence of the precession frequency, or a subharmonic, was found further downstream. They also found that the nozzle does not impart any significant net azimuthal velocity to the flow, although azimuthal gradients exist locally. More details of the near-field helical flow were identified by Nobes,[29] who measured the scalar (mixture fraction) field of a MPJ using a planar Mie scattering technique. He identified a vortex pair, presumably counterrotating in a manner analogous to a jet in crossflow, within the near-field helix. He concluded that the near-field helix "collapses" upon itself after approximately one turn of the helix for a wide range of St_p. Further downstream, the jet undergoes a transition to a state resembling a simple-jet flow.

These previous studies have increased our knowledge of the MPJ flow. Nevertheless, like its fluidic counterpart, this flow is extremely complex so that understanding of the turbulent mixing processes in it is still in its infancy. For example, measurements of velocity given by Schneider *et al.*[26–28] were limited to the region $x/d \leqslant 12$ and did not include energy frequency spectra nor a set of reliable high-order statistics such as skewness and flatness factors. Furthermore, previous measurements have phase averaged the flow relative to the rotation of the nozzle, rather than to the local position of the jet. That these local and phase-averaged trajectories can be quite different is evident from the planar images of Nobes.[29] To address these gaps in knowledge, the present study provides a more detailed investigation of the velocity field using a combined hot/cold-wire probe. The use of a cold-wire can minimize the directional ambiguity associated with a single hot-wire probe if the probe is carefully oriented relative to a known flow direction. Flow reversal is indicated by the measurement of a temperature rise by the coldwire. Importantly, the probe, although more poorly resolving flow direction, has significantly better spatial and temporal resolution than both LDA and particle image velocimetry (PIV). Hence it is well suited to provide measurements of frequency spectra and probability density functions of the fluctuating velocity. Some preliminary results of the present measurements have been reported in two conference papers by Mi *et al.*,[30,31] mainly for $\mathrm{St}_p = 0.02$. Here we present a more detailed and complete analysis of the velocity field in a MPJ flow. The specific aims of the present study are (1) to investigate the effect of St_p on the streamwise evolution of the flow in more detail and further downstream than has been done previously, (2) to characterize the dominant flow structure using a phase-averaging scheme based on the temporarily-determined local maximum of the instantaneous velocity over each cycle of precession, and (3) to extract detailed information of the near-field precessing jet based on this conditionally phase-averaged data.

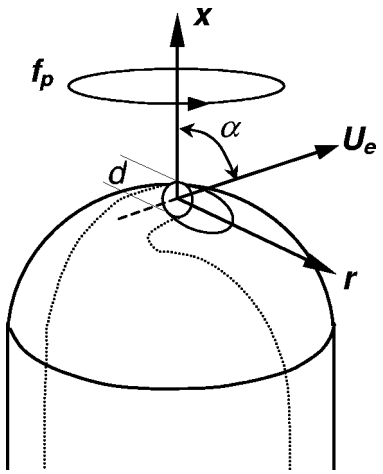

FIG. 1. A sketch of a rotating nozzle and the coordinate system.

II. EXPERIMENTAL DETAILS

A. Experimental conditions

The present study is performed using the mechanically rotating nozzle of Schneider *et al.*,[26–28] shown schematically in Fig. 1. This nozzle produces a well-defined initial flow in

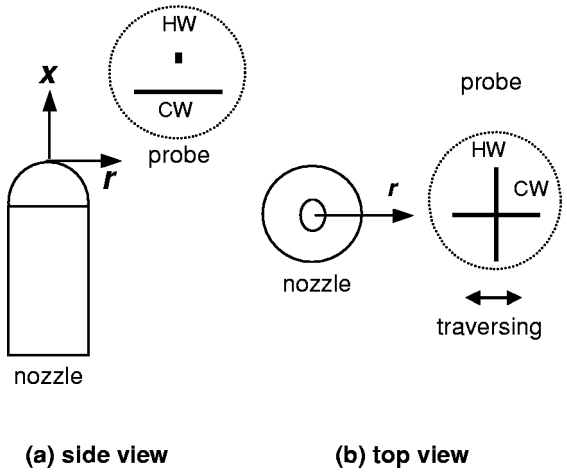

FIG. 2. The measuring probe vs the nozzle. Here, HW and CW denote "hot wire" and "cold wire," respectively.

which all of the parameters that characterize the flow field (i.e., the frequency of jet precession f_p, the nozzle exit diameter d, the jet-exiting angle α relative to the axis of rotation, the bulk exit velocity U_e, and the jet exit eccentricity) can be varied independently. The initial velocity profile at the nozzle exit for $\alpha=0$ is "top-hat" shaped.[26] The external tip of the nozzle is covered by a nonrotating shroud to prevent the external boundary layer of the rotating nozzle from exerting a significant influence on the flow. Likewise the rotating components of the motor and tooth belt are isolated from the jet flow by a cover-plate system.

For the present investigation, d is 10 mm, α is 45°, U_e is about 20 m/s, and the jet exit is centered on the axis of rotation. Correspondingly, the exit Reynolds number Re_d $(\equiv U_e d/\nu)$ is $\mathrm{Re}_d \approx 13\,300$. Three precession Strouhal numbers, i.e., $\mathrm{St}_p \approx 0.005$, 0.01, and 0.02 are investigated for which the corresponding values of rotating frequency, f_p, are 10, 20, and 40 Hz. The bulk exit velocity U_e is measured by a variable area flow-rate meter with an accuracy of ±2% and the frequency is controlled to an accuracy of ±0.1 Hz by a frequency-controlled 300 W electric motor.

B. Hot-wire anemometry

Hot-wire anemometry is used for the velocity measurements. The measuring probe, Fig. 2, combines a 5 μm tungsten hot wire, to measure velocity, and a 2.5 μm tungsten cold wire, to detect possible flow reversal by the thermal wake of the hot wire following Antonia *et al.*[32] The hot wire is oriented perpendicular to the cold wire. The hot wire is aligned and traversed radially, as shown in Fig. 2, based the phase-averaged measurements of Schnieder *et al.*[27] that were obtained with a three-component LDA. In this orientation the hot wire measures the projection of the total velocity in the (x,r) plane, i.e., $U=(V_x^2+V_r^2)^{1/2}$, where V_x and V_r are the axial and radial components of the total velocity. This orientation enables the cold wire to identify reversed flow for which $V_x<0$. The measurements of Ref. 27 show that for $\mathrm{St}_p \approx 0.015$ and $r/d \geqslant 2$, $|\langle V_r\rangle|/\langle V_x\rangle \approx 0.1-0.35$ at $x/d \geqslant 2$ and $|\langle V_\theta\rangle|/\langle V_x\rangle < 0.05$ at $x/d > 4$ (see their Fig. 19). This implies that overall $\langle U\rangle/\langle V_x\rangle \approx 100.5\%-106\%$. In other words, with the present orietation of the probe, the assumption that $\langle V_x\rangle \approx \langle U\rangle$ results in a minimum overestimation of about 6%. This is only slightly larger than the measurement uncertainty. Hence, the velocity-related results are presented in terms of U, noting that $\langle U\rangle \approx \langle V_x\rangle$.

The hot wire is operated at an overheat ratio of 0.8 by an in-house constant temperature circuit, while the cold wire is operated at 0.1 mA with an in-house constant current anemometer. The sign of the velocity component V_x is determined from the cold-wire signal when processing the data. Original signals from both wires are offset before being amplified, low-pass filtered at 2.8 kHz to eliminate high-frequency noise, and digitized at 5.6 kHz using a 12 bit A/D converter on a personal computer. The data record duration is about 30 s, a time that is sufficient for the spectral calculation. Calibration of the hot wire was carried out using a standard Pitot tube at the exit plane of a smoothly contracting round nozzle. It should be noted that measurements are limited to the region $x/d \leqslant 20-30$, depending the magnitude of St_p. Because reliable data are not possible beyond this region due to the rapid decay in jet velocity.

C. The conditional averaging scheme

In the present study, we performed the conditional averaging based on the temporally local maximum U_m, of instantaneous velocity signals over each cycle of precession. The mean and rms of U_m, i.e., $\langle U_m\rangle$ and $\langle u_m'\rangle = \langle (U_m - \langle U_m\rangle)^2\rangle^{1/2}$, were estimated at different radial locations in the region $1.5 \leqslant x/d \leqslant 10$. The average center of the jet is assumed to be located at $r=R_m$, which is the maximum of $\langle U_m\rangle$ across the entire measurement plane. We also choose $t=t_i$ as the origin of the phase angle, i.e., $\varphi = 2\pi(t-t_i)f_p$, where $t_i - 0.5f_p^{-1} \leqslant t \leqslant t_i + 0.5f_p^{-1}$ and the index i denotes the ith detection of U_m. Based on the same φ values varying between $-\pi$ and π, the phase averages of U and its fluctuating component are obtained over all the detected precession cycles within the measurement duration, forming the phase-averaged velocity mean and rms as below

$$\langle U|\varphi\rangle(r) = \frac{1}{N}\sum_{i=1}^{N} U_i(\varphi, r) \tag{1}$$

and

$$\langle u'|\varphi\rangle(r) = \left\{ \frac{1}{N}\sum_{i=1}^{N} [U_i(\varphi,r) - \langle U|\varphi\rangle(r)]^2 \right\}^{1/2}. \tag{2}$$

In (1) and (2), N is the total number of detections of U_m, which is about 300, 600, and 1200, respectively, for $f_p=10$, 20, and 40 Hz for the present measurements at $x/d \leqslant 7$. Note that, when $\varphi=0$, Eqs. (1) and (2) reduce to $\langle U|\varphi=0\rangle(r) = \langle U_m\rangle(r)$ and $\langle u'|\varphi=0\rangle(r) = \langle u_m'\rangle(r)$.

D. The experimental uncertainty

We have calculated experimental uncertainties for the measured quantities from estimated inaccuracies in the cali-

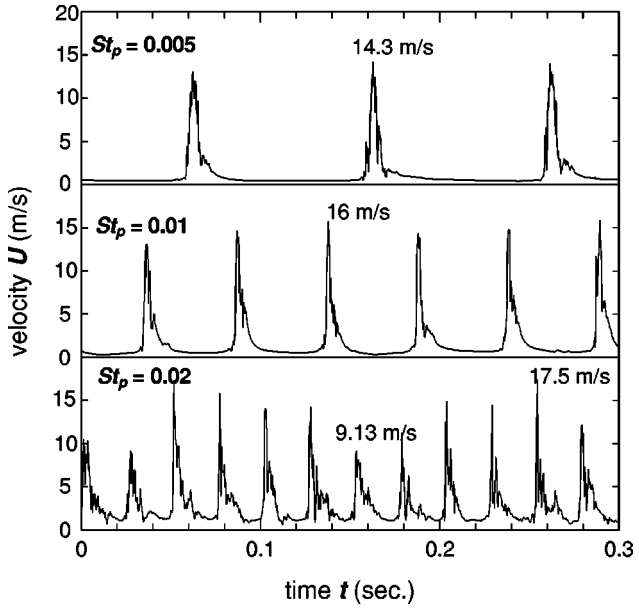

FIG. 3. Instantaneous velocity signals $U(t)$ for all three values of St_p obtained at $x/d=3$ and $r=r_m$.

bration data and particularly from the observed scatter in the measurements. The results are summarized as follows:

(1) *The unconditional time averages*: The uncertainty for the mean velocity is $[\langle U\rangle]\approx\pm1.5\%$ and that for the rms velocity is $[\langle u^2\rangle^{1/2}]\approx\pm2.0\%$.

(2) *The conditional averages*: The mean velocities $[\langle U|\varphi\rangle]$ and $[\langle U_m\rangle]$ are ±4.5% and ±3.5%, respectively, while the rms velocities $[\langle u_m'\rangle]$ and $[\langle u'|\varphi\rangle]$ are both $\approx\pm0.8\%$.

III. THE PRECESSING FLOW FIELD

Figure 3 shows the instantaneous velocity signals $U(t)$ for each of the three values of St_p measured at $x/d=3$ and $r=r_m$, i.e., the radius at which the local maximum of the time-averaged velocity $\langle U\rangle_m$ is found (details are presented later). Several features are evident. First, each cycle exhibits a rapid rise in the $U(t)$ followed by a much more gradual decrease. Each cycle is caused by the cyclical passage of the jet tangentially through the measurement probe, with the dominant frequency matching the frequency f_p (=10 Hz, 20 Hz, or 40 Hz) of rotation of the nozzle. The asymmetric nature of the rise and fall in $U(t)$ is consistent with the cross section of the jet being highly skewed, as found by Schneider *et al.*[27] It is also clear from Fig. 3 that there are cycle-to-cycle variations, with the peak magnitude U_m varying by up to a factor of 2 for $\mathrm{St}_p=0.02$.

A close check of the velocity signals for $r=r_m$ at all measured x/d suggests that precession of the flow field is still evident to a downstream distance of about $10d$, with some dependence upon St_p. This is verified unambiguously by the velocity power spectrum Φ_u, defined by $\int\Phi_u(f)df=\langle u^2\rangle$, where f is frequency. Figures 4 and 5, respectively, display the spectra obtained at $r=r_m$ and $r=0$ (the axis of rotation) in the region $1.5\leqslant x/d\leqslant15$. They demonstrate that a strong primary peak in Φ_u occurs at $f=f_p$, followed by a number of higher order harmonics when $x/d\leqslant7$. The strength of the primary and secondary peaks decrease rapidly in the range $7\leqslant x/d\leqslant10$. At $x/d=10$, several harmonics of the primary peak are still evident at both radial locations for $\mathrm{St}_p=0.005$ while only the primary peak is discernible at $r=r_m$ for $\mathrm{St}_p=0.02$. This implies that the rate of decay in significance of the precession increases with St_p. For $x/d\geqslant15$, none of the spectra exhibit any distinct peak at any discrete frequency relating to the precession. It follows that there exists a transition region which separates the upstream region, in which the entire flow oscillates at the frequency of precession, from the downstream region, where it does not. For all the three values of St_p, the onset of the transition region is located between $x=10d$ and $x=15d$. As further deduced from Figs. 4 and 5, the exact location slightly upstream with an increase in St_p. This dependence on St_p is consistent with the concentration measurements of Nobes.[29]

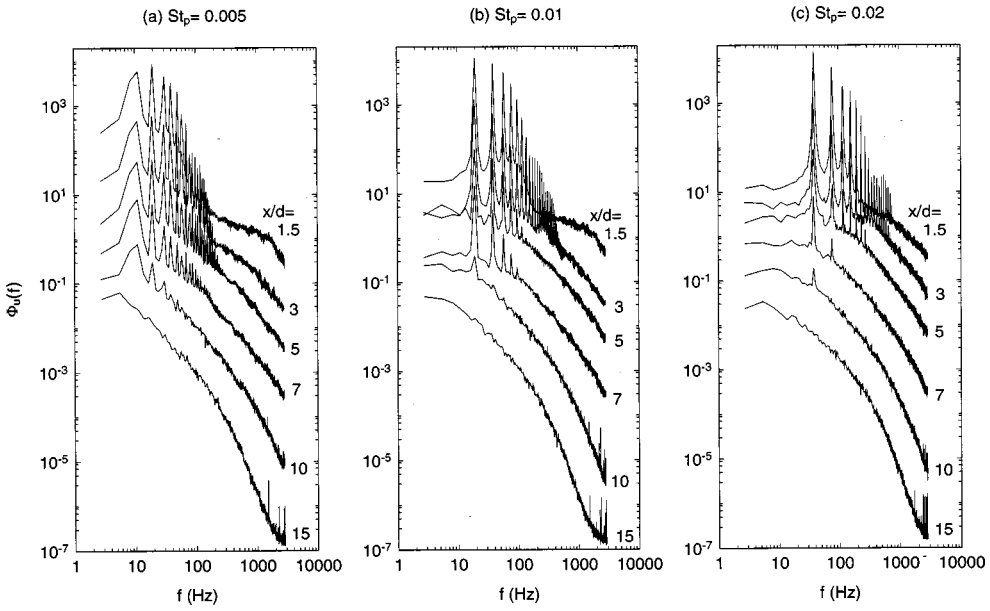

FIG. 4. Frequency spectra $\Phi_u(f)$ of the fluctuating velocity u obtained at $r=r_m$ in the region from $x/d=1.5$ to $x/d=15$.

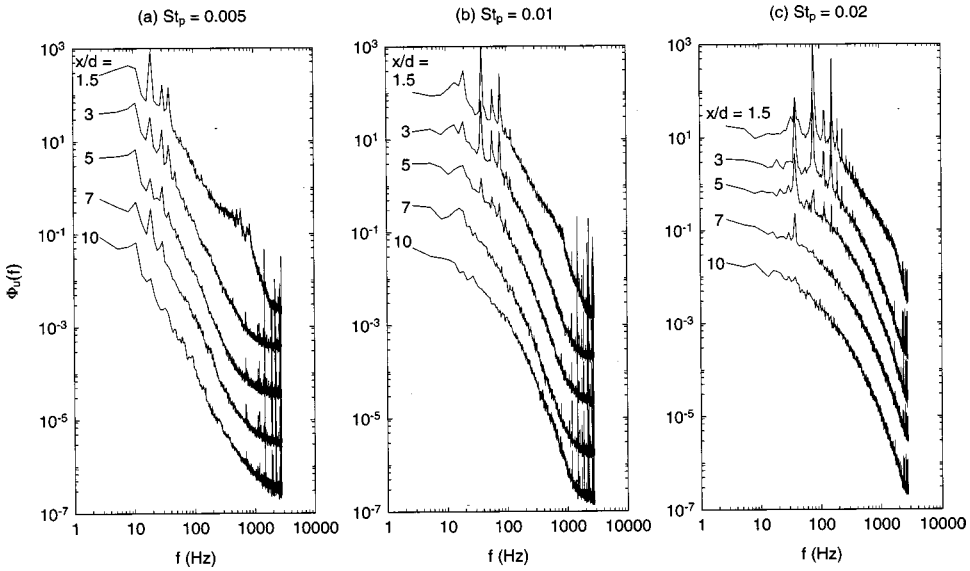

FIG. 5. Frequency spectra $\Phi_u(f)$ of the fluctuating velocity u obtained at $r=0$ in the region from $x/d=1.5$ to $x/d=10$.

It is interesting to compare the location of the transition region determined by the present method with that obtained in Ref. 27 where the researchers phase averaged their LDA measurements based on mechanical triggering from the location of the nozzle. They deduced the end of the upstream precessing region to be $x/d\approx 6$ for $\mathrm{St}_p\approx 0.015$, which is much closer to the nozzle than the present values of $x/d \approx 12$. This difference suggests that the instantaneous trajectory of the precessing flow exhibits a substantial deviation from the previous phase-averaged value (which is necessarily linked directly to the phase of the rotating nozzle), the extent of which increases with the downstream distance.

IV. CONVENTIONAL STATISTICS OF THE PRECESSING JET FLOW

Figures 6(a) and 6(b) show the axial evolution of the radial distributions of the convetional time-averaged velocity $\langle U\rangle$ and rms velocity fluctuation $u'\equiv\langle u^2\rangle^{1/2}$, normalized by U_e, in the region $1.5\leqslant x/d\leqslant 20$ for $\mathrm{St}_p=0.005$, 0.01, and 0.02. Both figures use the same scales to assist in comparisons. Consistent with the trends measured in Refs. 27 and 28, Fig. 6(a) identifies a central recirculation zone in the time-averaged flow for all the values of St_p in the region $1.5 \leqslant x/d\leqslant 7$. The size of the central recirculation zone increases as St_p decreases, while the magnitude of the maximum reverse velocity decreases with decreasing St_p. However, Schneider *et al.*[27,28] reported a shorter zone than determined here from Fig. 6(a). The radial profiles of their time-averaged axial velocity component, their Fig. 19(a), suggest that the mean reverse flow is located in the region $x/d\leqslant 6$.

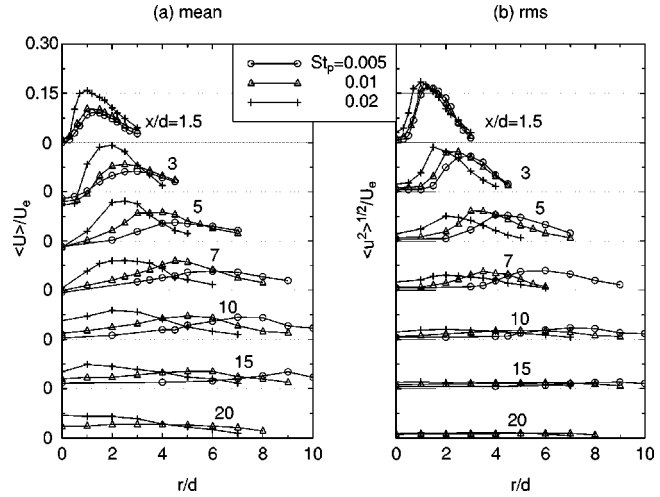

FIG. 6. Radial distributions of the normalized time-averaged velocity and rms fluctuation for $\mathrm{St}_p=0.005$, 0.01, and 0.02. (a) The mean $\langle U\rangle/U_e$; (b) the rms u'/U_e, where $u'\equiv\langle u^2\rangle^{1/2}$.

Figure 6(a) also shows that, as expected, the time-averaged velocity decays much faster than a nonprecessing jet flow. For example, at $x/d=15$, the local maximum of $\langle U\rangle$, denoted by $\langle U\rangle_m$, is only 7.5% of U_e for $\mathrm{St}_p=0.02$ and less than 5.5% for both $\mathrm{St}_p=0.005$ and 0.01. By comparison, $\langle U\rangle_m/U_e$ is greater than 40% at the same relative downstream distance in the nonprecessing round jet (presented later in Fig. 20). The low level of the time-averaged velocity is caused, at least to a great extent, by the high initial entrainment of low-velocity ambient flow induced by the precession in the near field for $x/d<15$ (see Fig. 13).

Figure 7 shows the fraction (γ) of time occupied by the precessing jet, obtained at the locations for the local maximum velocity $\langle U\rangle_m$, corresponding to the local jet center. The criterion used to determine the time occupied by the jet was $U\geqslant 0.1U_M$, where $U_M=\max\{U(t)\}$. As expected, the value of γ increases with St_p and x/d and asymptotes to unity at the location where the jet converges to the nozzle axis. The asymptotic value of $\gamma\approx 1$ has been gained at $x/d\geqslant 15$ for $\mathrm{St}_p=0.01$ and 0.02. However, for $\mathrm{St}_p=0.005$ the value of γ is below unity through the measured region. This low fraction (thus high intermittency of induced ambient fluid) in the near field results in the rms velocity u' being comparable with the mean $\langle U\rangle$. Indeed, the magnitude of u' is greater than that of $\langle U\rangle$ in the region $x/d\leqslant 3$ [Figs. 6(a) and 6(b)]. Bearing this in mind, the magnitude of u' in the near-field region should

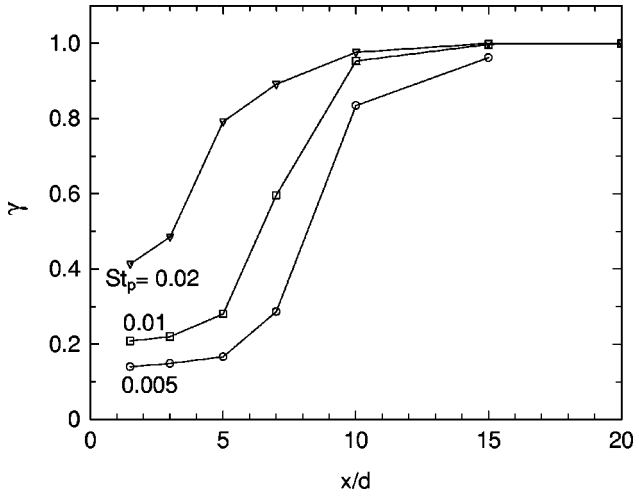

FIG. 7. The fraction of time (γ) occupied by the precessing jet fluid at $r = r_m$.

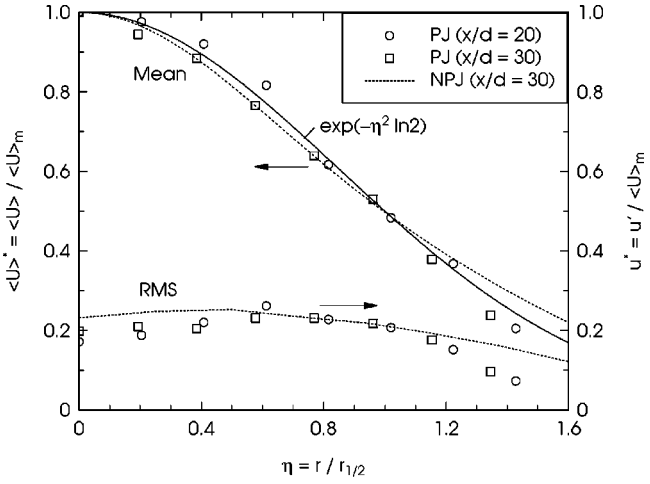

FIG. 9. Radial profiles of $\langle U\rangle/\langle U\rangle_m$ and $u'/\langle U\rangle_m$ for $\mathrm{St}_p=0.02$ obtained at $x/d=20$ and 30.

not be regarded as the measure of turbulence intensity of the local jet flow. Further evidence of the transition to a more conventional "fully developed jet" flow with axial distance can be seen by comparing the ratio of the rms to the mean. In the region $x/d \geqslant 15$, the normalized rms, $u'/\langle U\rangle_m$, for $\mathrm{St}_p = 0.02$ is found to match reasonably well with the far-field value of a nonprecessing jet (Fig. 9). (Note that this "far-field" comparison is not meant to suggest that the far field completely forgets the near-field precession—later results show that this is clearly not the case). A gradual transition between the near-and far-field values is evident in the intervening region.

It is also instructive to assess the effect of variations in St_p on the radial component of the trajectory of the time-averaged jet in the near field. It is clear from Fig. 6(a) that the radial location of the peak in the mean velocity depends strongly on St_p, suggesting that the trajectory does so as well. Further details of the trajectory can be found in Fig. 8 which presents the radial location r_m of the maximum local velocity

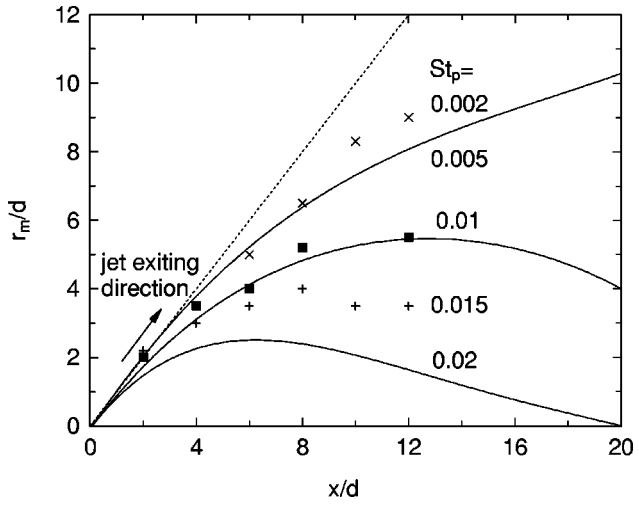

FIG. 8. The radial location r_m of the maximum mean velocity $\langle U\rangle_m$. Present: best-fit curves. Schneider [Ref. 26]: symbols.

$\langle U\rangle_m$. It is clear that two different classes of trajectory exist. For $\mathrm{St}_p=0.005$, r_m increases monotonically with x and the radial trajectory never converges to the axis of rotation. In contrast, for $\mathrm{St}_p=0.01$ and 0.02, r_m increases first and then decreases until it becomes zero, suggesting the presence of a critical Strouhal number separating two regimes (this issue is to be discussed in more detail later).

Figure 8 also demonstrates that the present measurements of the radial trajectory agree reasonably well with those earlier reported by Schneider[26] for $\mathrm{St}_p=0.002$, 0.01, and 0.015, although his measurements were obtained only for $x/d \leqslant 12$. The two independent measurements of r_m for the same value of $\mathrm{St}_p=0.01$ are in close agreement, despite the somewhat different Reynolds numbers ($\mathrm{Re}_d=13\,500$ for the present flow versus $\mathrm{Re}_d=26\,600$ for Schneider's flow). This is consistent with previous investigations on nonprecessing round jets where the effects of Re_d are found to be negligible for $\mathrm{Re}_d > 10\,000$ (e.g., Refs. 33 and 34). It is also consistent with previous work for precessing jet flows where it is found that Re_d has a much weaker influence on the characteristic features of the flow than does St_p.[24,26,29]

Figure 9 shows the radial profiles of $\langle U\rangle/\langle U\rangle_m$ and $u'/\langle U\rangle_m$ obtained at $x/d=20$ and 30 for the case of $\mathrm{St}_p=0.02$. For comparison, the corresponding profiles for a circular nonprecessing jet obtained at $x/d=30$ are also presented on the plot. Here $\eta=r/r_{1/2}$ and $r_{1/2}$ is the half-velocity radius at which $\langle U\rangle=0.5\langle U\rangle_m$. The fact that both the normalized mean and rms profiles at $x/d=20$ agree reasonably well with those at $x/d=30$ suggests that the flow is approaching a fully developed state at $x/d>30$. Further evidence for this is found in the collapse of the centerline velocity spectra Φ_u, here normalized by x and $\langle U\rangle_m$ for $x/d=20$ and 30 (Fig. 10).

Importantly, the far-field profiles of $u'/\langle U\rangle_m$ (Fig. 9) and spectra of u (Fig. 10) for $\mathrm{St}_p=0.02$ differ significantly from those of the nonprecessing jet case, even though the mean values for both cases are reasonably well described by the Gaussian distribution $\langle U\rangle/\langle U\rangle_m=\exp(-\eta^2\ln 2)$. This is consistent with the knowledge that different initial and upstream boundary conditions propagate downstream. Previous studies

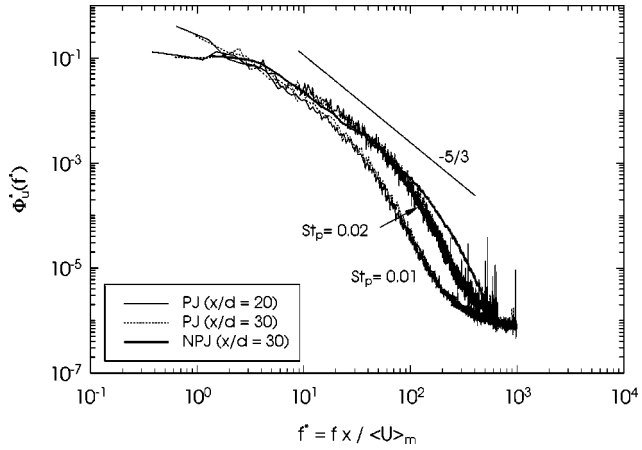

FIG. 10. The centerline velocity spectra $\Phi_u(f)$ normalized by x and $\langle U\rangle_m$ obtained at $x/d=20$ and 30.

(e.g., Refs. 34 and 35) have demonstrated that different initial conditions have influence on the entire scalar field of a circular jet, so that a multiplicity of self-preservation can and does occur.

Several other important issues can be observed from the spectral data shown in Fig. 10. It is evident that, in addition to the $St_p=0.02$ case, there is also a good collapse for $St_p=0.01$ at $x/d=20$ and 30. However, the normalized distributions of Φ_u for the two values of St_p are distinct and also different from that for the nonprecessing jet. First, there is less high-frequency energy for the precessing than for the nonprecessing jet, and this difference becomes more significant as St_p decreases. This implies that the upstream jet precession results in a redistribution of the turbulence scales, i.e., the simultaneous increase in large-scale mixing and decrease in small-scale turbulence generation. This redistribution depends upon the Strouhal number. Second, there appears to be a power-law region in the spectrum, i.e., $\Phi_u \sim f^{-m}$, apparently for all the cases with the exponent $m \approx 1.45$ being about identical. However, the extent of this power-law region is clearly wider for the nonprecessing jet. In addition, the value of $m=1.45$ is quite different from the well-known Kolmogorov value of $5/3(\approx 1.67)$, as noted previously in Ref. 36.

Figure 11 shows the influence of the precessing Strouhal number St_p on the probability density function (PDF) of the fluctuating velocity $p(u)$ measured at $r=r_m$. Here, $p(u)$ is defined by $\int_{-\infty}^{+\infty} p(u)du=1$ and $\int_{-\infty}^{+\infty} u^n p(u)du=\langle u^n\rangle$. In the near field the PDF is highly spiked and slightly bimodal. However, the shape of $p(u)$ changes dramatically with x/d, evolving to a nearly Gaussian distribution at $x/d=20$. The evolution toward a Gaussian distribution occurs more rapidly with increased St_p. The transition to Gaussian distribution accompanies the transition to fully developed turbulence and reflects the decaying significance of the precession and the increased significance of fine-scale turbulence. To further investigate the transition to fully developed turbulence at $r=r_m$, Fig. 12 compares the skewness $S_u \equiv \langle u^3\rangle/\langle u^2\rangle^{3/2}$ and flatness $F_u \equiv \langle u^4\rangle/\langle u^2\rangle^2$ of u measured at $r=r_m$. Data is presented for different Strouhal numbers including the case for the nonprecessing round jet ($\alpha=0$; $r=0$). The Gaussian values ($S_u=0$ and $F_u=3$) are also indicated for reference. Several observations can be made from Figs. 11 and 12.

(1) In the near field at $x/d \leqslant 10$, the global precession (large-scale motion) controls the turbulent statistics. As a result, the shape of $p(u)$, characterized by S_u and F_u, for the precessing jet is very different from that for the nonprecessing jet. The turbulent statistics for the nonprecessing jet along the centerline become approximately Gaussian at $x/d \geqslant 8$. In contrast, the near-field skewness in the PJ flow is as high as 3.8 and the flatness as high as 17.

(2) The shape of the PDF, as characterized by S_u and F_u, depends strongly on St_p. The lower the value of St_p, the higher the values of both S_u and F_u and the further the departure from Gaussian statistics. This reflects a tightening of

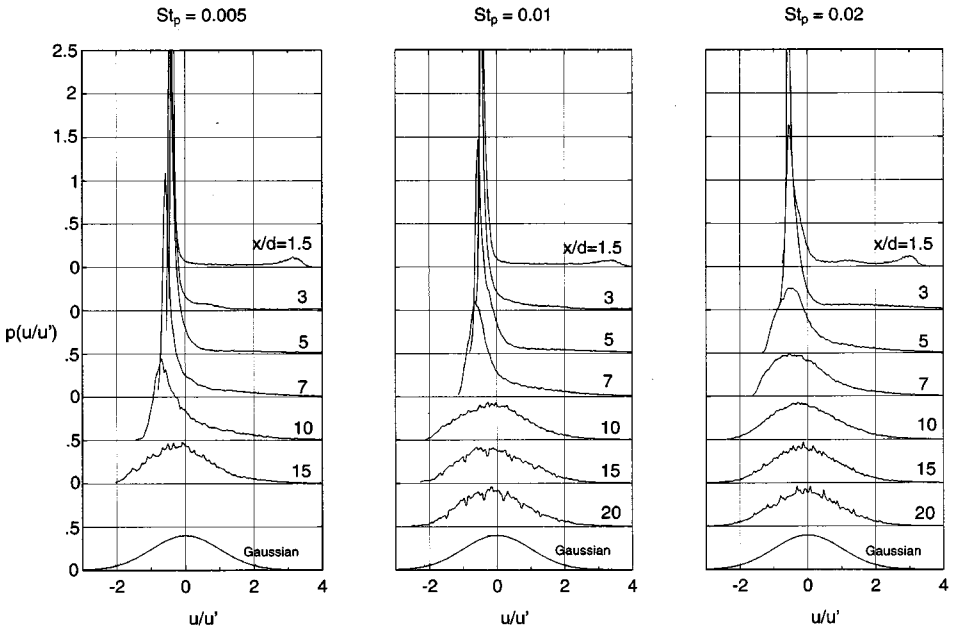

FIG. 11. Probability density function (PDF) $p(u)$ of the fluctuating velocity u obtained at $r=r_m$.

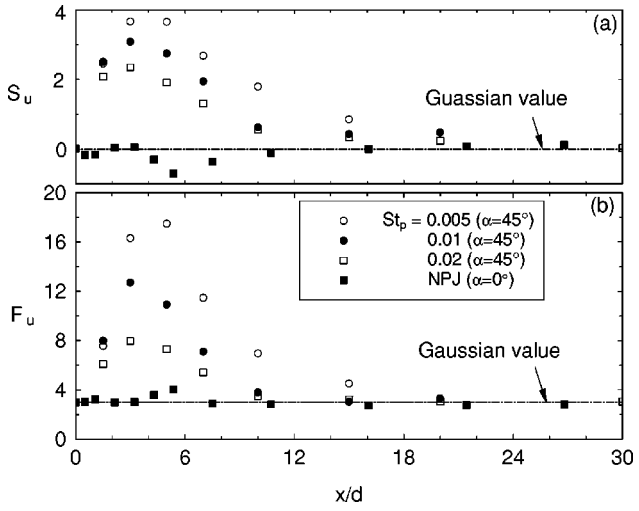

FIG. 12. Axial variations of the skewness $S_u \equiv \langle u^3 \rangle / \langle u^2 \rangle^{3/2}$ and flatness $F_u \equiv \langle u^4 \rangle / \langle u^2 \rangle^2$ obtained at $r = r_m$ for precessing jets at different Strouhal numbers and $r = 0$ for the nonprecessing round jet ($\alpha = 0$).

the near-field helix with increased St_p. For example, the PDF of u at $r = r_m$ for $St_p = 0.02$ evolves to a distribution not far from Gaussian at $x/d = 10$, while it may occur much farther downstream for $St_p = 0.005$.

(3) For $St_p = 0.01$ and 0.02, the PDF in the flow region at $x/d \geqslant 15$ becomes nearly Gaussian along the axis of rotation and are indistinguishable from the nonprecessing jet. For $St_p = 0.005$, the statistics trend toward Gaussian values at $r = r_m$, although conclusive results could not be obtained with the present technique due to the mean velocity being too low beyond $x/d = 15$.

V. CONDITIONAL PHASE-AVERAGED STATISTICS OF THE PRECESSING JET FLOW

To examine the near-field region of the local precessing jet flow, contours are presented of both the phase-averaged mean velocity $\langle U | \varphi \rangle$ and rms velocity $\langle u' | \varphi \rangle$ for $x/d = 1.5$, 3, and 5. These can be seen in Figs. 13–15 for $St_p = 0.005$, 0.01, and 0.02, respectively. The dimensionless abscissa and ordinate are r/d and $\varphi R_m/d$. Here R_m is the radial distance between the local jet center and the axis of rotation (see Fig. 22) so that φR_m represents the mean tangential distance traversed by the jet center corresponding to an arc angle of φ.

It is evident from contours of $\langle U | \varphi \rangle$ (left-hand side) that the cross section of the core region of the precessing jet is approximately elliptical in shape at $x/d \leqslant 1.5$ for all values of St_p. This is due, in part, to the fact that the cross section of the "slice" is perpendicular to the axis of rotation rather than to the local jet centerline, which is initially aligned at 45° to it. However, the shape of the cross section is increasingly distorted from its initial ellipsoid with downstream distance and forms a strong "tail" by $x/d = 5$, features also observed in Ref. 26. The axial distance required to achieve a given extent of distortion increases with St_p, as can be seen from comparison between the contours of $\langle U | \varphi \rangle (r)$ for different Strouhal numbers, Figs. 13–15. For the highest Strouhal number $St_p = 0.02$, the elliptical shape is distorted even at $x/d = 1.5$ and the long tail of the jet is evident from $x/d = 3$.

The presence of a wake-like tail has been observed in other related flows, such as a jet in a cross flow (e.g., Ref. 37), even though aspects of the underlying mechanisms may be different. The wake-like tail behind a jet in a cross flow contains a "vortex bubble."[37] Similar features in the tail following the precessing jet can be observed from Figs. 13–15 of Ref. 27 for $St_p = 0.015$, although the presence of the vortex bubble was not discussed by the authors. It is evident too from their Fig. 19 that significantly negative values of the tangential mean velocity occur between $r/d = 0.5$ and 2.5 in the near-field region at $x/d \leqslant 6$. Planar measurements of concentration by Nobes,[29] using the Mie scattering technique, also provide evidence of a vortex pair, presumably counter-rotating in a manner analogous to a jet in cross flow.

Figures 13–15 also present the phase-averaged rms $\langle u' | \varphi \rangle$ (right-hand side). In contrast to a nonprecessing jet, the near-field rms of the precessing jet is far from axisymmetric. Instead, it exhibits two peaks, located tangentially "in-front of" and "behind" the jet center. The front peak is stronger than the rear peak (also see Fig. 18). This is consistent with physical reasoning in which it can be expected that the precession would act to increase the strain rate tangentially along the front edge of the jet and also, to a lesser extent, behind the jet center. The locations of the two peaks correspond approximately to those at which the gradient $\partial \langle U | \varphi \rangle / \partial r$ is maximum. With an increase in either x/d or St_p, the two peaks merge and decay. For example, for $St_p = 0.02$ the double peaks have been replaced by a single peak at $x/d = 5$ (Fig. 15). In contrast, this transition occurs at $x/d \approx 10$ for $St_p = 0.005$ and $x/d \approx 7$ for $St_p = 0.01$ (not shown here).

More details of the velocity-field development can be found in Fig. 16 which shows the radial distributions of the normalized mean (upper) and rms (lower) velocity, $\langle U_m \rangle / U_e$ and $\langle u_m' \rangle / U_e$, obtained at $1.5 \leqslant x/d \leqslant 10$. Note that $\langle U_m \rangle = \langle U | \varphi = 0 \rangle$ and $\langle u_m' \rangle = \langle u' | \varphi = 0 \rangle$. Clearly, the conditionally averaged velocity is much higher than the unconditionally time-averaged value in the near field [see Fig. 6(a)], but the differences reduce in the far field. It is of interest to note that the mean profile shapes on the outer side of the local jet ($r > R_m$) for all tested values of St_p have a similar shape to that for the nonprecessing jet while the profile on the inner side is very different. This can be demonstrated clearly in Fig. 17 (upper) by plotting the renormalized data $\langle u_m^* \rangle^* = \langle u_m' \rangle (r) / \langle U_m \rangle (r = R_m)$ against $\eta = (r - R_m)/Y_{1/2}^{+r}$. Here $Y_{1/2}^{+r}$ is the half-width on the outer side of the jet, i.e., $\langle U_m \rangle (Y_{1/2}^{+r}) = \frac{1}{2} \langle U_m \rangle (R_m)$ determined in the radial direction for $r > R_m$. For comparison, the Gaussian distribution $\exp(-\eta^2 \ln 2)$, a close approximation of the far-field distribution of $\langle U \rangle / U_c$ for the nonprecessing counterpart, is also included in the plots. It is evident that the profile of $\langle U_m \rangle^* (\eta)$ for $\eta > 0$ obtained in the region at $3 \leqslant x/d \leqslant 10$ closely follows the Gaussian distribution for all the values of St_p. Upstream at $x/d = 1.5$, the measurement is within the potential core region of the jet, as is discussed later in more detail, so that $\langle U_m \rangle^* (\eta)$ is not expected to follow the Gaussian distribution. Moreover, the Strouhal number has a significant impact on the overall shape of the $\langle U_m \rangle$ profile. As St_p increases, not

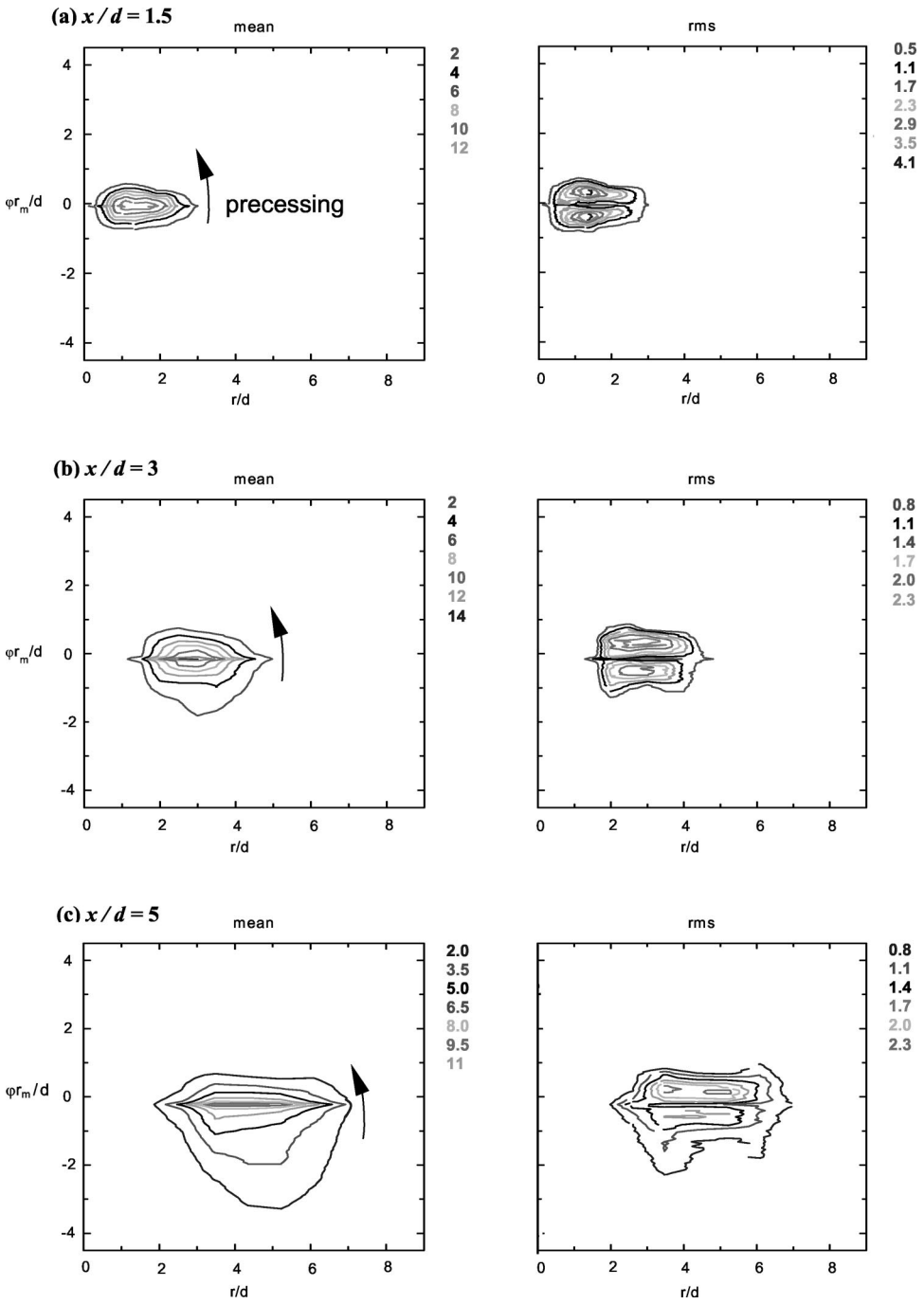

FIG. 13. Contours of the phase-averaged mean velocity $\langle U|\varphi\rangle(r)$ and rms velocity fluctuations $\langle u'|\varphi\rangle(r)$ obtained at $x/d=1.5$, 3, and 5 for $\mathrm{St}_p=0.005$.

only does the radial position (R_m) of the maximum of $\langle U_m\rangle$ moves closer to the axis, but also the near-axis side of the profile becomes steeper.

Similar to the nonprecession case, the radial rms profiles $\langle u_m'\rangle^*=\langle u_m'\rangle(r)/\langle U_m\rangle(r=R_m)$ for the precessing jet, Fig. 17 (lower), exhibit a double-peak pattern, although two peaks are not symmetric with respect to the local jet center. This is, in part, due to the fact that the plane of the measurement is not perpendicular to the axis of the local jet in the near field. For comparison, Fig. 17 (lower) also presents by dashed lines the nonprecession case with normalization by the local maximum on the centerline, i.e., $\langle u^2\rangle^{1/2}/U_c$. The data for the nonprecessing jet were obtained at $x/d=3$, 10, and 30. In the near-field region at $x/d\leqslant 3$, the relative rms for $\mathrm{St}_p=0.005$ is close to that for the nonprecessing jet. As the flow proceeds further downstream, the relative rms increases more rapidly in the precessing jet than in the nonprecessing jet. For $\mathrm{St}_p=0.01$ and 0.02, Figs. 17(b) (lower) and 17(c) (lower), the axial increase in $\langle u_m'\rangle^*$ becomes more pronounced. It appears that the rms level increases as St_p increases. Nevertheless, it should be noted that, since an appropriate calculation of $\langle u_m'\rangle$ requires a much larger number of samples of U_m, namely, N in Eqs. (1) and (2), than does that of $\langle U_m\rangle$, the uncertainty of $\langle u_m'\rangle$ is certainly far greater than the latter. Therefore, the accuracy of $\langle u_m'\rangle$ is limited.

Figure 18 shows the normalized tangential distributions of the velocity mean (upper) and rms (lower) through the

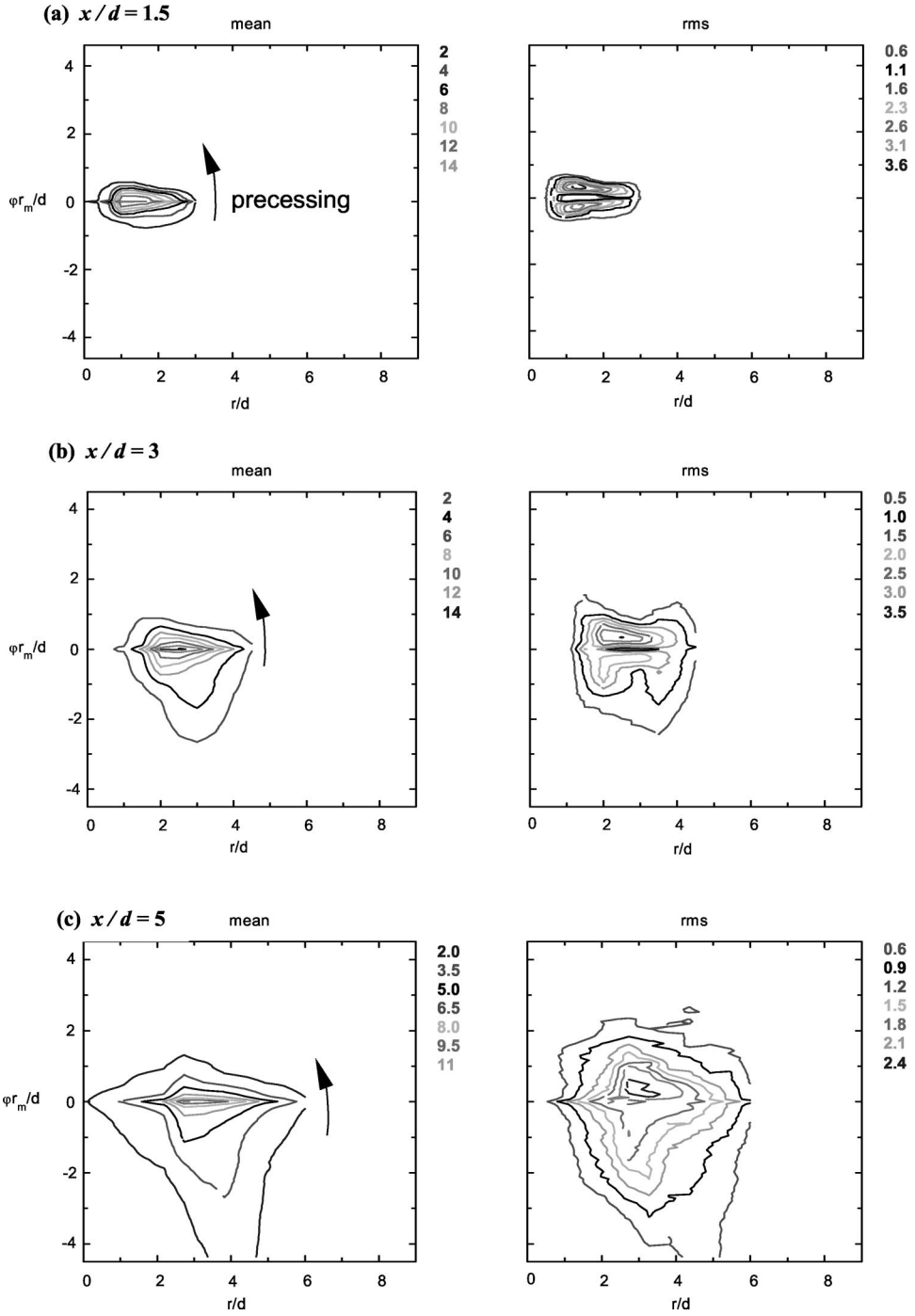

FIG. 14. Contours of the phase-averaged mean velocity $\langle U|\varphi\rangle(r)$ and rms velocity fluctuations $\langle u'|\varphi\rangle(r)$ obtained at $x/d=1.5$, 3, and 5 for $\mathrm{St}_p=0.01$.

local jet center, i.e., $(\langle U|\varphi\rangle/\langle U|\varphi=0\rangle)_m$ and $(\langle u'|\varphi\rangle/\langle U|\varphi=0\rangle)_m$ against $\varphi R_m/d$, for $x/d=1.5$, 3, 5, and 7. As expected, the distributions change significantly with increasing downstream distance. It is also seen that the Strouhal number has a significant impact on the distributions. The rms profile peaks both in front and behind the jet center at $x/d=1.5$–5 for $\mathrm{St}_p=0.005$ and 0.01 while showing double peaks only when $x/d\leqslant 3$ for $\mathrm{St}_p=0.02$. In general, the front peak is stronger than the rear one and this difference becomes more significant as St_p increases. It is interesting that the front peak appears to persist throughout the near-field region and its magnitude varies only slightly for $\mathrm{St}_p=0.01$ and 0.02. Even the rear peak value (0.18–0.27, 0.18–0.2, and 0.16–0.18 for $\mathrm{St}_p=0.005$, 0.01, and 0.02) is obviously greater than the equivalent value (0.08–0.14) for the nonprecessing jet over the same region at $x/d\leqslant 7$. At $x/d=1.5$, the local rms-peak values are substantially higher along the tangential than radial direction, due to the effect of precession. At further distances downstream, $x/d=7$, the peak occurs only in front of the jet center, with a value close to that for the radial profile, reflecting a reduced significance of the local precession.

Figures 19(a)–19(c) show the radial profiles of the local maximum of the instantaneous velocity, $U_M=\max\{U$ over the entire data record$\}$ for $\mathrm{St}_p=0.005$, 0.01, and 0.02, respectively, obtained in the region $1.5\leqslant x/d\leqslant 15$. It is interesting

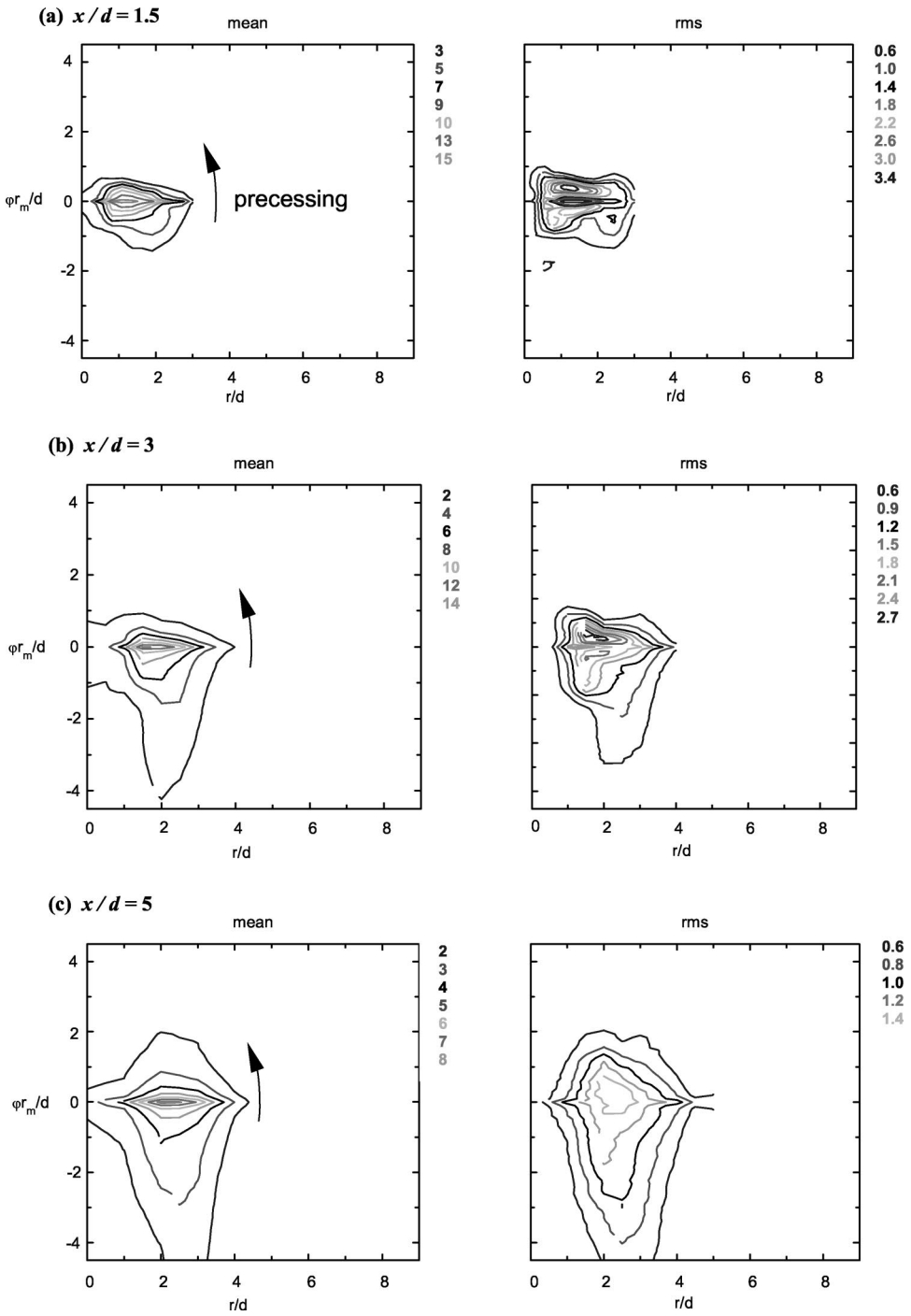

FIG. 15. Contours of the phase-averaged mean velocity $\langle U|\varphi\rangle(r)$ and rms velocity $\langle u'|\varphi\rangle(r)$ obtained at $x/d=1.5$, 3, and 5 for $\mathrm{St}_p=0.02$.

to compare the profiles of U_M/U_e with those of $\langle U_m\rangle/U_e$ shown in Fig. 16. They are broadly similar in shape and of greater magnitude as expected. However, there is an important difference in their axial evolutions. As x increases, while $\langle U_m\rangle$ decreases monotonically, U_M first increases and then decreases rapidly downstream from $x/d\approx 3$. This difference becomes more significant at higher Strouhal numbers. To investigate this difference in more detail, Fig. 20 compares the axial variations of local maxima of $U_M(r)$, Fig. 20(a), and $\langle U_m\rangle(r)$, Fig. 20(b), for both the precessing and nonprecessing jet flows. The maximum value is obtained over all radii, i.e., $\langle U_m\rangle(R_m)$ and $U_M(R_M)$, for the three Strouhal numbers, where R_m and R_M are the radial locations of maxima of $\langle U_m\rangle$ and U_M, respectively. For the nonprecessing jet ($\alpha=0°$), these are assumed to occur on the centerline, denoted by $\langle U_c\rangle$ and U_{cM}.

As demonstrated in Fig. 20(a), U_{cM} increases continuously from $x/d=0$ to $x/d=3$ by about 40%. This is due to the behavior of vortex rings that are generated from the roll-up of the initial axisymmetric vorticity sheet formed from the smoothly contracting inside wall upstream of the nozzle exit. The occurrence of these coherent vortical rings is indicated by the primary peak present in the spectrum Φ_u (not shown here). These rings wrap around the central potential core, move downstream, and interact with each other, thereby spreading the vorticity. As a result of their mutual interac-

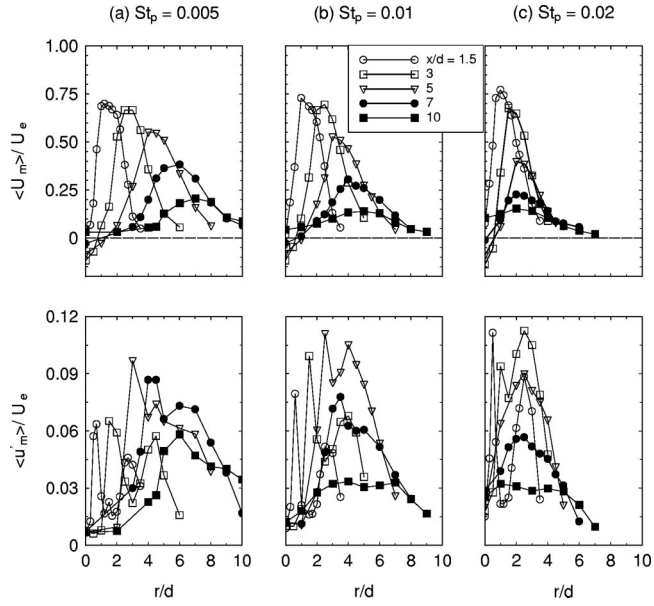

FIG. 16. Radial distributions of the normalized conditional-averaged mean (upper) $\langle U_m\rangle(r)/\langle U_m\rangle(R_m)$ and rms (lower) $\langle u_m'\rangle(r)/\langle U_m\rangle(R_m)$ obtained at $1.5\leqslant x/d\leqslant 10$.

tion, the vortices merge at some downstream distance at $x/d\geqslant 2$. During a period of time when vortex pairings occur, two adjacent in-phase ring-like vortices roll around each other while moving downstream, thereby speeding up the local flow so that $U_{cM}>U_e$ even though $\langle U_c\rangle\approx U_e$. It has been shown in Grinstein *et al.*[38] that in their simulated circular jet ($\mathrm{Re}_d\sim 150\,000$), the axial instantaneous maximum velocity steadily increases along the potential core region, reaching the highest value, i.e., $U_c=U_{cM}$, at $x/d\approx 3.5$ [see their Fig. 3.2.1(c)]. The steady growth of U_M until $x/d<3$ observed in the present precessing jets should also suggest the occurrence of the ring-like vortices in the near region of these flows. Indeed, these vortices have been seen evidently in Fig. 4.2 of Schneider,[26] who used the laser-induced fluorescence (LIF) technique to visualize the precessing jet in a water tank facility. (Note, however, that the existence of these vortices is difficult to be detected in the power spectrum of u due to the high intermittency of ambient flow induced by the precession.) In addition, Fig. 20(a) also demonstrates that the near-field growth rate of U_M increases with St_p. The reason for this is that, as St_p increases, the included angle between the local velocity vector and the axis of rotation decreases and, consequently, the axial velocity component increases.

Figures 20(a) and 20(b) demonstrate that both local velocities $U_M(R_M)$ and $\langle U_m\rangle(R_m)$ of the precessing jet decay substantially faster than do the equivalents U_{cM} and $\langle U_c\rangle$ of the nonprecessing jet at $x/d\leqslant 15$. This implies that the oscillation of the entire jet promotes entrainment of the ambient fluid. The phase-averaged centerline measurements of the local jet obtained by Schneider[26] for $\mathrm{St}_p=0.01$ and 0.015 are also shown in Fig. 20(b) for comparison. As discussed earlier, his data were obtained using a different phase-averaging technique, based on the reference phase of the nozzle rotation identified at the exit plane over multiple cycles, which does not necessarily sample the local maxima for the calculation of $\langle U_m\rangle$. It is therefore not surprising that the $\langle U_m\rangle\times(R_m)/U_e$ data of Ref. 26 are consistently lower than the present data at the same Strouhal number (e.g., $\mathrm{St}_p=0.01$). We note that this difference is unlikely to result from the difference in Re_d used by the two studies ($\mathrm{Re}_d=13\,300$ versus $\mathrm{Re}_d=26\,600$) because, as indicated earlier, the influence of Re_d is not significant, at least between these two values of

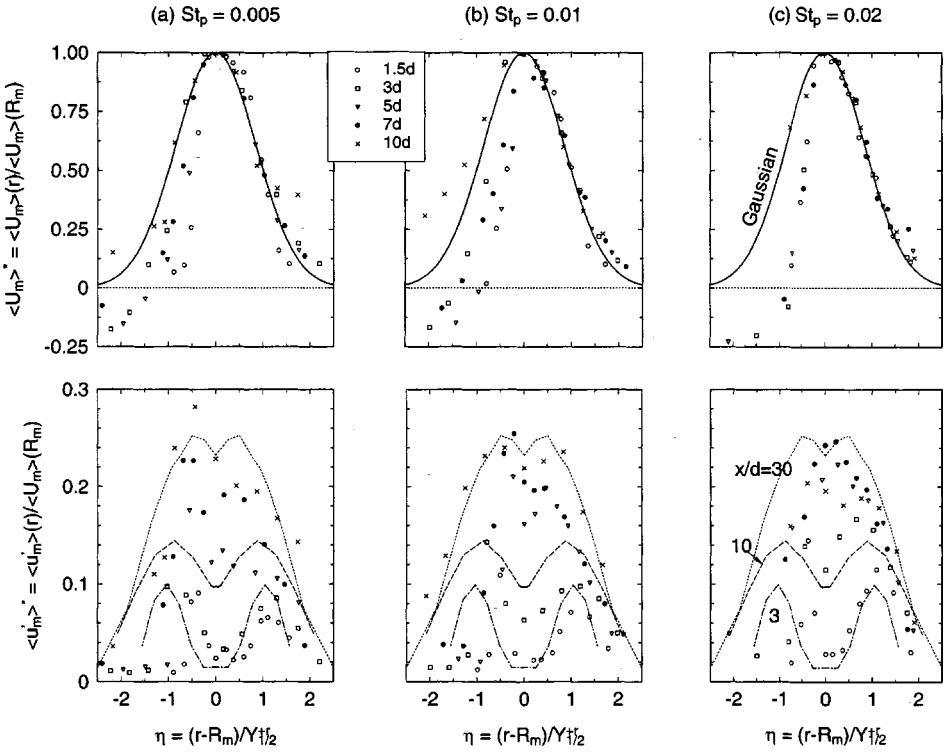

FIG. 17. Radial distributions of the normalized conditional-averaged mean (upper) $\langle U_m\rangle(r)/\langle U_m\rangle(R_m)$ and rms (lower) $\langle u_m'\rangle(r)/\langle U_m\rangle(R_m)$ obtained at $1.5\leqslant x/d\leqslant 10$. In the lower plots, dashed-lines represent the rms data for the nonprecessing jet.

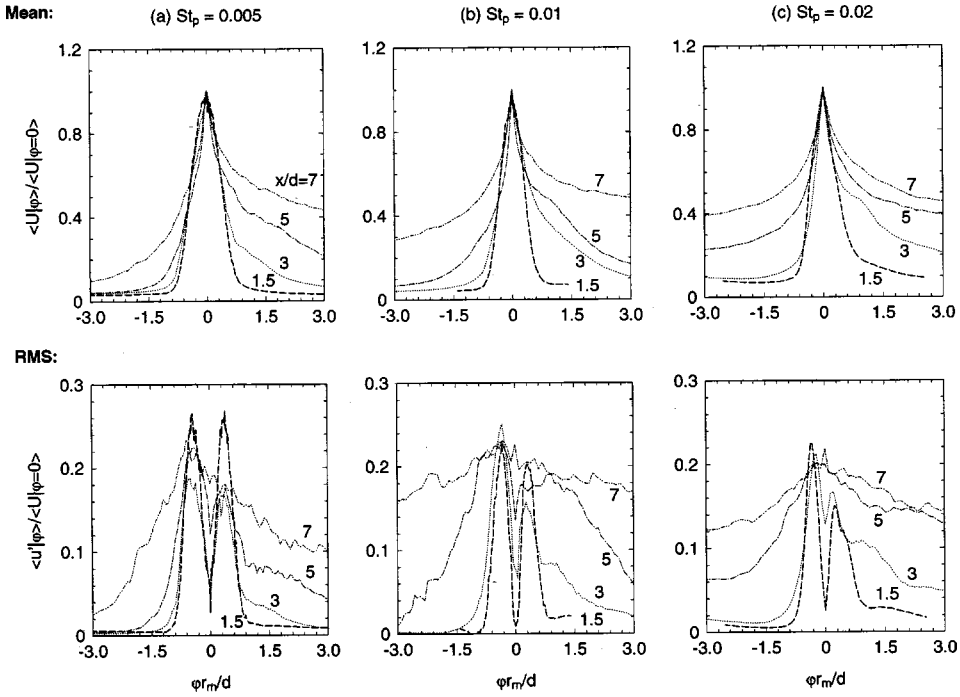

FIG. 18. Tangential distributions of the normalized velocity mean (upper) and rms (lower), $(\langle U|\varphi\rangle/\langle U|\varphi=0\rangle)_m$ and $(\langle u'|\varphi\rangle/\langle U|\varphi=0\rangle)_m$.

Re_d. Moreover, the present data of $\langle U_m\rangle(R_m)$ for $\mathrm{St}_p=0.005$ agrees reasonably well at $x/d\geqslant 5$ with that of Wong *et al.*[22] for a naturally fluidic precessing jet (FPJ) confined in a cylindrical chamber ($\mathrm{Re}_d=84\,500$). In the FPJ case, the initial jet exiting angle of $\alpha=0$ results in quite different values of $\langle U_m\rangle(R_m)/U_e$ for $x/d<5$. Their Strouhal number was estimated to be $\mathrm{St}_p\approx 0.002$ (not given in Ref. 22). Note also that their phase-averaged measurements were based on a pressure signal from a reference probe located near to the chamber outlet.

Consistent with an increase in the velocity decay rates, the averaged half-width $Y_{1/2}$ of each precessing jet grows more rapidly than does the half-radius $R_{1/2}$ of the nonprecessing round jet. This is clearly demonstrated in Fig. 21. Here we have calculated the "average" half-width as follows:

$$Y_{1/2}=\tfrac{1}{4}(Y_{1/2}^{-r}+Y_{1/2}^{+r}+Y_{1/2}^{-\varphi}+Y_{1/2}^{+\varphi}), \tag{3}$$

where $Y_{1/2}^{-r}$ and $Y_{1/2}^{+r}$ are the half-widths in the radial direction, while $Y_{1/2}^{-\varphi}$ and $Y_{1/2}^{+\varphi}$ are those in the tangential direction, on either side of the jet center ($\varphi=0$). All of these half-widths are measured from the local jet center. It should be noted that the path length of the precessing jet L_T has been calculated based on the trajectory path of the local centreline of the jet. This trajectory is curved rather than a straight line. Figure 21 also suggests an increase in the overall spreading rate of the precessing jet when St_p increases from 0.005 to 0.02. This

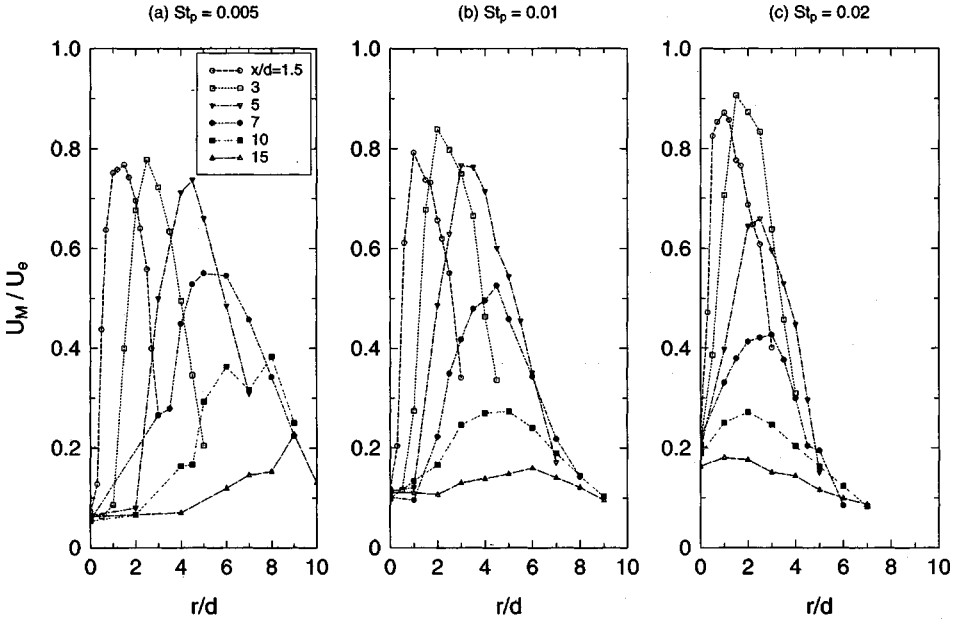

FIG. 19. Radial profiles of the local maximum velocity $U_M=\max\{U_m$ over all precession cycles$\}$ obtained in the region $1.5\leqslant x/d\leqslant 15$.

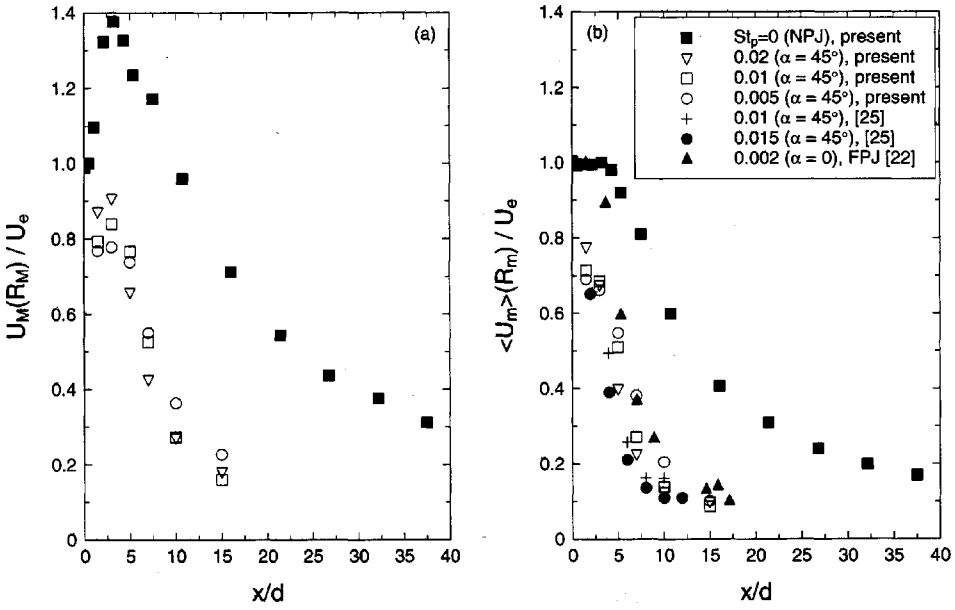

FIG. 20. Axial variations of local maxima of (a) $U_M(R_M)$ and (b) $\langle U_m\rangle \times(R_m)$ for the precessing jet and the centerline $\langle U_c\rangle$ and U_{cM} for the non-precessing jet ($\alpha=0°$).

coincides with the St_p dependence of the velocity decay rate observed in Fig. 20.

We now investigate the trajectory of the conditionally averaged jet centerline to capture the "instantaneous" feature of the precessing jet. Here the trajectory is defined as the locus of those locations at which the conditionally averaged velocity maximum occurs. The angular position φ can be estimated from the axial and radial locations of the trajectory (x_m, R_m) along with the precessing frequency f_p and $\langle U_m\rangle$, via

$$\varphi = 2\pi f_p(t-t_0) = 2\pi f_p \int_0^x \langle U_m\rangle^{-1}(x)dx,$$

where $(t-t_0)$ is the time taken by the nozzle fluid "particles" for passing a downstream distance of x. The above equation may be rewritten in a normalized form as

$$\varphi = 2\pi St_p \int_0^{x/d} (\langle U_m\rangle/U_e)^{-1} d(x/d). \tag{4}$$

The integral in (4) can be obtained from the experimental data of $\langle U_m\rangle/U_e$ reported in Fig. 20(b). Figure 22 shows the axial variation of the radial location R_m of the trajectory. For comparison, the corresponding locations R_M and r_m for the radial maxima of U_M and the time-averaged velocity $\langle U\rangle$ are also included, as is the initial direction of the jet. It is apparent that all data sets from three definitions of trajectory, based on R_m, r_m, and R_M, agree reasonably well, although not perfectly. Importantly, the data provides more evidence of the presence of a "critical" Strouhal number. For low Strouhal numbers at, say, $St_p \leqslant 0.005$, the radial component of the trajectory continually diverges from the axis of rotation. In contrast, for the higher Strouhal numbers, $St_p \geqslant 0.01$, the trajectory of the local jet eventually converges with the axis of rotation. According to this graph, for the case of $\alpha=45°$, the critical Strouhal number $St_{p,cr}$ occurs between $St_p=0.005$ and

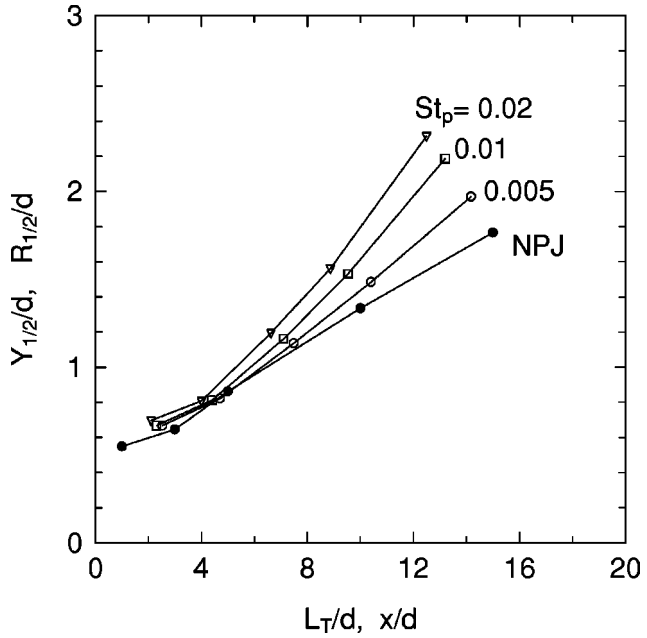

FIG. 21. Axial variations of the averaged half-width $Y_{1/2}$ of the precessing jets for $St_p=0.005$, 0.01, and 0.02.

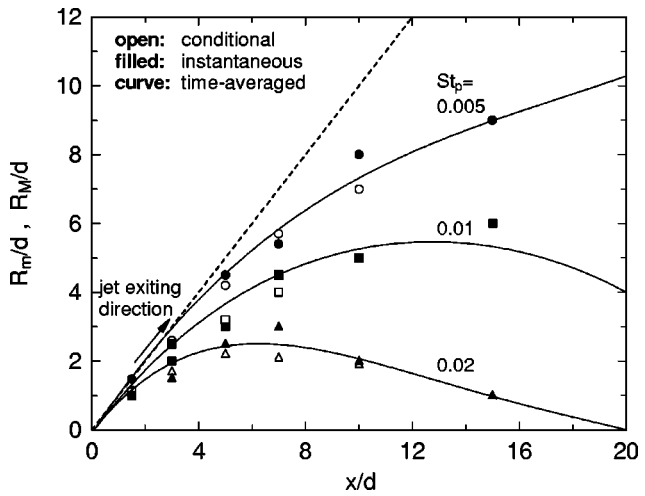

FIG. 22. Axial variations of the radial locations of the maxima of $\langle U_m\rangle(r)$ and $U_M(r)$, denoted by R_m and R_M.

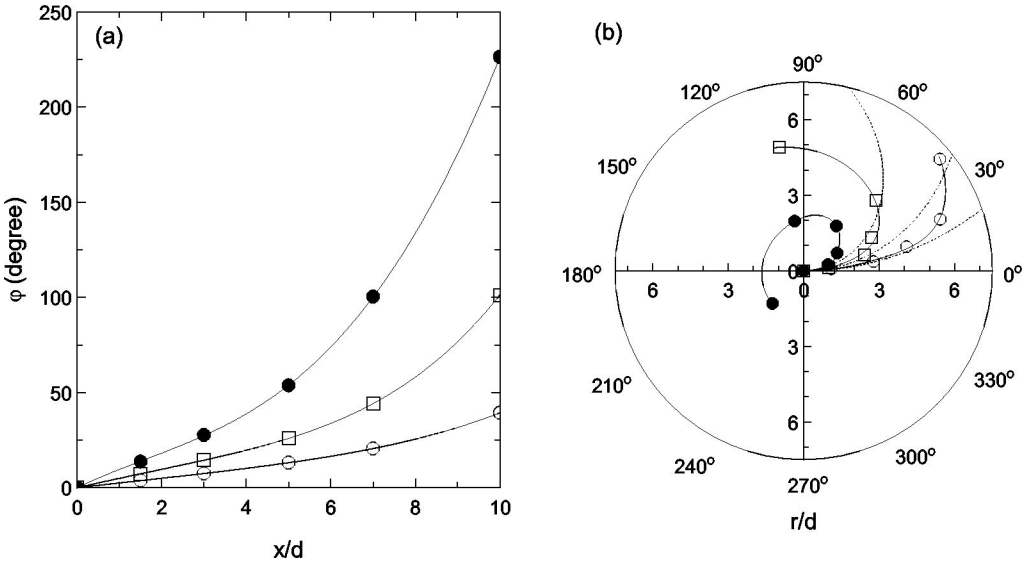

FIG. 23. Mean trajectory of the precessing jet center. (a) In rectangular coordinates, (b) in polar coordinates.

$St_p = 0.01$ at an estimated value of $St_{p,cr} \approx 0.008$.

The angular component of the trajectory φ is presented for each Strouhal number in Fig. 23, both in terms of the axial variation [Fig. 23(a)] and the tangential variation [Fig. 23(b)]. One important observation is that, even for the case of $St_p = 0.02$, the trajectory at $x/d \leqslant 10$ undergoes less than one full helical turn of the jet (i.e., $\varphi < 2\pi$) before it "merges" with itself or the spiral-like structure has "collapsed" to be indistinguishable from the mean flow. (Refer back to the velocity spectra in Fig. 4.) Specifically, the magnitude of the trajectory arc in the region $x/d \leqslant 10$ is $\varphi \approx 2\pi/9$, $5\pi/9$, and $11\pi/9$, respectively, for $St_p = 0.005$, 0.01, and 0.02. Hence, under subcritical conditions ($St_p < 0.01$) the extent of angular "deflection" of the jet trajectory in the near field is less than 90°, which can be deduced to be too small to enable direct interaction of the jet itself at different phases of the cycle. As a result, the central recirculation zone is weak in strength and large in size for $St_p = 0.005$ and the negative pressure within it is insufficient to modify the jet trajectory significantly (Ref. 26 and Fig. 22). In contrast, the angular "deflection" in supercritical conditions is substantially greater than 90° and is evidently large enough for different phases of the jet helix to interact strongly and merge until the jet begins to entrain itself forming a strong recirculation with a low-pressure central core region.[26]

VI. FURTHER DISCUSSION

In the preceding sections, we have reported both conditionally and unconditionally statistical properties of the velocity field in a MPJ flow with the precession Strouhal number varying between $St_p = 0.005$ and $St_p = 0.02$. We have also compared the MPJ results with those of a circular jet (not precessing). For the MPJ flow, owing to the variation of St_p, not only have significant differences been identified in the near-field precession-dominated region ($x/d \leqslant 10$) but also nonidentical states of the turbulent velocity field have been observed in the far field. Here, we propose to relate these differences in statistics to the differences in the underlying structure.

The underlying structure of the MPJ is quite different from that of a nonprecessing round jet issuing from a smoothly contracting nozzle which has been well investigated elsewhere. The physical picture for the nonprecessing jet may be described as follows. When the jet is discharging into a stagnant surroundings, a shear layer is formed immediately downstream from the nozzle and then an early linear instability region develops, involving exponential growth of small perturbations of the velocity profile. As the flow proceeds downstream, the nonlinear Kelvin–Helmholtz instability occurs, inducing the roll-up of vorticity, forming ring-like vortices (large-scale coherent structures). Subsequently, the merging or pairing of the rings occurs. Further downstream, the ring-like structures break down due to their strong interactions with each other and with induced ambient fluids, thus followed by the transition region. In the far-field region, new type of coherent structures have developed, as demonstrated by a large body of previous investigations (e.g., Refs. 39–42). The far-field coherent structures are mainly in the helical mode[40] and present almost all the time.[42]

The MPJ flow may also be divided into three regions: the near-field, transition, and far-field regions. However, these regions differ significantly from those of the nonprecessing jet. In the near-field region, the path of the emerging jet forms a three-dimensional helix-like structure which precesses with respect to the nozzle axis. This can be unequivocally confirmed by two-dimensional phase-averaged images of concentration of Nobes,[29] and may also be deduced from Figs. 4, 5, and 23(b). When the Strouhal number exceeds $St_{p,T}$, a threshold (<0.005), the strength of precession becomes high enough to form a central recirculation zone (CRZ) in which the pressure is lower than ambient. As St_p increases further, the CRZ pressure lowers further[26] and the "helix" is pulled closer to the nozzle axis (Fig. 22). Since the occurrence of precession increases the large-scale interaction

between the jet and ambient fluids and thus large-scale entrainment, the rms (i.e., fluctuating intensity), the decay rate and the half-width of the phase-averaged velocity field are all increased in this region relative to the nonprecessing counterpart (Figs. 17, 20, and 21). These properties also increase with increasing St_p.

The near-field region ends where the precessing helix-like structure entrains itself or "collapses." The flow then undergoes a transition to a far-field state that resembles some features of a nonprecessing jet. Within the transition region, there is a rapid decay in any features associated with the entire-jet precession. The occurrence of the precession results in large "engulfment" of ambient fluid into the spaces between the different phases of the helical jet. Although within the envelope of the jet volume, this fluid is not truly mixed with the original jet fluid. Such mixing occur mainly in the transition region. The concentration measurements of Nobes[29] suggest that the flow in this region is characterized by "layering" remnants of the helical structure collapsed. His measurements also demonstrated high values of the concentration gradient in the layers surrounding the remnants and the low magnitude of the mean concentration across the flow. It appears from Fig. 7 that, as St_p increases the transition region shifts upstream.

The far-field structure configuration also depends on the Strouhal number. When St_p is below or above the critical value $St_{p,cr}$ (≈ 0.008 for the present case), the jet core is located off or centrally around the nozzle axis (Fig. 6). That is, in the subcritical regime the initially precessing jet does not develop to a nonprecessing-jet-like flow, while in the supercritical regime the jet does. For $St_p > St_{p,cr}$, the starting point of the nonprecessing-jet-like region moves upstream as St_p increases (Fig. 22). In this context, we can conclude that the underlying structure of turbulence in the far-field region is different under different Strouhal numbers. Even in the supercritical regime, while the overall structure of turbulence in the far field tends toward that of the nonprecessing jet, detailed characteristic behaviors are not all identical with those of the latter and also not all the same at different Strouhal numbers. In other words, the residual effect of the precession is still significant in the nonprecessing-jet-like region. This is well supported by comparison of the centerline velocity spectra (Fig. 10) which demonstrate that the existence of precession redistributes turbulence scales relative to the nonprecessing case. Furthermore, as St_p decreases, the contribution to the kinetic energy from large scales grows, while that from small scales falls.

VII. CONCLUSIONS

Using the hot-wire anemometry, the present study has investigated a mechanical precessing air jet, initially exiting into stagnant air surroundings at an angle of $\alpha = 45°$ with respect to the axis of rotation of the nozzle. Three significantly different values of the Strouhal number of precession, i.e., $St_p \approx 0.005$, 0.01, and 0.02, have been tested to assess the impact of St_p on the downstream flow development. It has been found that, in general, the Strouhal number has significant influence on the entire mixing field of the MPJ flow. More specifically, several conclusions can be made from the present study.

(1) The MPJ flow has a regime of globally coherent precession at $x/d \leqslant 10-15$ (depending upon St_p). When the Strouhal number exceeds a threshold (<0.005 for the present case), the strength of precession becomes high enough to enable the formation of a CRZ in the near field. As the Strouhal number increases from the threshold, the CRZ pressure lowers and consequently the CRZ size decreases while the reverse flow velocity increases.

(2) Use of the conditionally phase-averaging scheme, which is based on the local instantaneous maximum over each cycle of precession, has been able to extract some important characteristics of the precessing jet in the near-field region at $x/d \leqslant 10$. It is found, for example, that the jet is "squashed" on the front side in the direction of precession so that its shape in cross section changes from an initial circle to a largely deformed ellipse, with a long tail reflecting the existence of a trailing counterrotating vortex pair. The strain rate is increased tangentially on the front side of the jet and also, to a lesser extent, on the trailing side. Correspondingly, the rms of the conditional velocity within the jet exhibits a strong peak in the leading edge and a weak peak behind the jet center.

(3) The precessing jet itself behaves like a three-dimensional helix until the structure has broken down at $x/d = 10-15$ (depending on St_p). However, the jet, even for $St_p = 0.02$, can only undergo less than a complete helix turn before the collapse of the precession.

(4) The occurrence of precession promotes the interaction between the jet and ambient fluids and thereby increases large-scale mixing. As a result, the relative fluctuation intensity (i.e., normalized rms), decay rate, and half-width of the conditional velocity field of the precessing jet are all considerably increased in the region at $x/d \leqslant 10-15$, relative to the nonprecessing counterpart (Figs. 17, 20, and 21). These properties increase with increasing St_p.

(5) Despite enhancing large-scale entrainment of the ambient fluid, the occurrence of precession concurrently suppresses the generation of the fine-scale turbulence (and thus the molecular-level mixing). Hence, the spectrum of turbulence scales is redistributed from that of the nonprecessing counterpart. That is, the precession leads to an increase in the fraction of contributions of large and small scales to the kinetic energy of turbulence. The redistribution becomes less significant as the Strouhal number increases.

(6) For the present case (the initial jet deflection angle $\alpha = 45°$), the critical Strouhal number is around $St_p = 0.008$. At lower values the mean flow never behaves like a nonprecessing jet, whereas at higher values it develops eventually into a regime in the far field where it resembles some features of the nonprecessing counterpart. The flow for $St_p = 0.02$ appears to become fully developed at $x/d \geqslant 30$. It is anticipated that, at higher values of St_p the jet should attain the fully developed state at smaller downstream distances.

ACKNOWLEDGMENTS

The authors gratefully acknowledge the support of the Australian Research Council and the Fuel Combustion Technology Pty through the Linkage Grant Scheme.

[1] N. Syred and J. M. Beer, "Combustion in swirling flows: A review," Combust. Flame **23**, 143 (1974).
[2] E. Gutmark, T. P. Parr, D. M. Hanson-Parr, and K. C. Shadow, "On the role of large and small-scale structure in combustion control," Combust. Sci. Technol. **66**, 107 (1989).
[3] W. G. Hill, Jr. and P. R. Greene, "Increased turbulent jet mixing rates observed by self-excited acoustic oscillations," J. Fluids Eng. **103**, 520 (1977).
[4] M. Piatt and H. Vietts, "Conditional sampling in an unsteady jet," AIAA Pap. 79–1857, 1979.
[5] J. M. Simmons, J. C. S. Lai, and M. F. Platzer, "Jet excitation by an oscillating vane," AIAA J. **19**, 673 (1981).
[6] J. M. Simmons, M. F. Platzer, and T. C. Smith, "Velocity measurements in an oscillating plane jet issueing into a moving air stream," J. Fluid Mech. **84**, 33 (1978).
[7] G. J. Nathan, "The enhanced mixing burner," Ph.D. thesis, Department of Mechanical Engineering, The University of Adelaide, 1988.
[8] S. C. Crow and F. H. Champagne, "Orderly structure in jet turbulence," J. Fluid Mech. **48**, 547 (1971).
[9] E. Gutmark and C. M. Ho, "On the preferred modes and spreading rates of jets," Phys. Fluids **26**, 2932 (1983).
[10] J. G. Cervantes and V. W. Goldschmidt, "The apparent flapping motion of a turbulent plane jet—Further experimental results," J. Fluids Eng. **103**, 119 (1981).
[11] R. E. Luxton, G. J. Nathan, Luminis Pty. Ltd., "Mixing using a fluid jet," US Patent No. 5 060 867 (1991).
[12] G. J. Nathan, S. J. Hill, and R. E. Luxton. "An axisymmetric 'fluidic' nozzle to generate jet precession," J. Fluid Mech. **370**, 347 (1998).
[13] G. J. R. Newbold, G. J. Nathan, D. S. Nobes, and S. R. Turns, "Measurement and prediction of NO_x emissions from unconfined propane flames from turbulent-jet, bluff-body, swirl and precessing jet burners," Proc. Combust. Inst. **28**, 481 (2000).
[14] J. J. Parham, G. J. Nathan, J. P. Smart, S. J. Hill, and B. G. Jenkins, "The relationship between heat flux and NO_x emissions in gas fired rotary kilns," J. Inst. Energy **73**, 25 (2000).
[15] C. G. Manias and G. J. Nathan, "The precessing jet gas burner—A low NO_x burner providing process efficiency and product quality improvements," World Cem. **24** (3), 4 (1993).
[16] C. G. Manias and G. J. Nathan, "Low NO_x clinker production," World Cem. **25** (4), 54 (1994).
[17] C. G. Manias, G. J. Nathan, and D. S. Rapson, "Gyro-Therm: A new efficient low NO_x gas burner for product quality improvement," ASEAN Federation of Cement Manufacturers, Kuala Lumpar, April, 1995.
[18] R. Videgar, "Gyro-Therm technology solves burner problems," World Cem. **28** (11), 39 (1997).
[19] N. L. Smith, G. J. Nathan, D.-K. Zhang, and D. S. Nobes, "The significance of particle clusters in pulverised coal flames," Proc. Combust. Inst. **29**, 797 (2002).
[20] N. L. Smith, N. P. Megalos, G. J. Nathan, and D.-K. Zhang, "The role of fuel rich clusters in flame stabilization and NO_x emission reduction with precessing jet p.f. flames," Proc. Combust. Inst. **27**, 3173 (1998).
[21] G. J. Nathan and S. J. Hill, "Full scale assessment of the influence of a precessing jet of air on the performance of pulverized coal flame in a cement kiln," Sixth European Conference on Industrial Furnaces and Boilers (INFUB), Lisbon, Portugal, 2–5 April 2002.
[22] C. Y. Wong, P. V. Lanspeary, G. J. Nathan, R. M. Kelso, and T. O'Doherty, "Phase-averaged velocity in a fluidic precessing jet nozzle and in its near external field," Exp. Therm. Fluid Sci. **27**, 515 (2003).
[23] C. Y. Wong, G. J. Nathan, and R. M. Kelso, "Velocity measurements in the near field of a fluidic precessing jet flow using PIV and LDA," *Third Australian Conference on Laser Diagnostics in Fluid Mechanics and Combustion*, December 2–3, Brisbane, Australia.
[24] J. Mi and G. J. Nathan, "Self-excited jet-precession Strouhal number and its influence on downstream mixing field," J. Fluids Struct. **19**, 851 (2004).
[25] G. J. Nathan, S. R. Turns, and R. V. Bandaru, "The influence of jet precession on emissions and radiation from turbulent flames," Combust. Sci. Technol. **112**, 211 (1996).
[26] G. M. Schneider, "Structures and turbulence characteristics in a precessing jet flow," Ph.D. thesis, Department of Mechanical Engineering, University of Adelaide, Australia, 1996.
[27] G. M. Schneider, D. Froud, N. Syred, G. J. Nathan, and R. E. Luxton, "Velocity measurements in a precessing jet flow using three dimensional LDA system," Exp. Fluids **23**, 89 (1997).
[28] G. M. Schneider, G. J. Nathan, R. E. Luxton, J. D. Hooper, and A. R. Musgrove, "Velocity and Reynolds stresses in a precessing jet," Exp. Fluids **22**, 489 (1997).
[29] D. S. Nobes, "Structures and turbulence characteristics in a precessing jet flow," Ph.D. thesis, Department of Mechanical Engineering, University of Adelaide, Australia, 1998.
[30] J. Mi, G. J. Nathan, and R. E. Luxton, "Frequency spectra of turbulence in a precessing jet," *Proceedings of the Seven Asian Congress of Fluid Mechanics*, December 8–12, 1997, Madras, India.
[31] J. Mi, R. E. Luxton, and G. J. Nathan, "The mean velocity field of a precessing jet," *Proceeding of 13th Australasian Fluid Mechanics Conference*, December 13–18, 1998, Melbourne, Australia.
[32] R. A. Antonia, A. J. Chambers, and A. K. M. F. Hussain, "Errors in simultaneous measurements of temperature and velocity in the outer part of a heated jet," Phys. Fluids **23**, 871 (1980).
[33] P. Dimotakis, "The mixing transition in turbulent flows," J. Fluid Mech. **409**, 69 (2001).
[34] J. Mi, D. S. Nobes, and G. J. Nathan, "Influence of jet exit conditions on the passive scalar field of an axisymmetric free jet," J. Fluid Mech. **432**, 91 (2001).
[35] W. K. George, "The self-preservation of turbulent flows and its relations to initial conditions and coherent structures," in *Advance in Turbulence*, edited by W. K. George and R. E. A. Arndt (Hemisphere, New York, 1989), pp. 39–73.
[36] J. Mi and R. A. Antonia, "Effect of large-scale intermittency and mean shear on scaling range exponents in a turbulent jet," Phys. Rev. E **64**, 026302 (2001).
[37] T. F. Fric and A. Roshko, "Vortical structure in the wake of a transverse jet," J. Fluid Mech. **148**, 405 (1994).
[38] F. F. Grinstein, M. N. Glauser, and W. K. George, "Vortex in jets," in *Fluid Vortices*, edited by S. I. Green (Kluwer Academic, Dordrecht, 1995).
[39] W. J. A. Dahm and P. E. Dimotakis, "Mixing at large Schmidt number in the self-similar far field of turbulent jets," J. Fluid Mech. **217**, 299 (1990).
[40] J. Tso and F. Hussain, "Organized motions in a fully developed turbulent axisymmetric jet," J. Fluid Mech. **203**, 425 (1989).
[41] M. G. Mungal and J. M. O'Neil, "Visual observation of turbulent diffusion flames," Combust. Flame **78**, 377 (1989).
[42] M. Yoda, L. Hesselink, and M. G. Mungal, "The evolution and nature of large-scale structures in the turbulent jet," Phys. Fluids A **4**, 803 (1992).